NAVAL POSTGRADUATE SCHOOL

MONTEREY, CALIFORNIA

THESIS

MEMS UNDERWATER DIRECTION FINDING ACOUSTIC SENSOR

by

German Eduardo Da Re

September 2018

Thesis Advisor: Gamani Karunasiri
Co-Advisor: Fabio D. Alves

THIS PAGE INTENTIONALLY LEFT BLANK

REPORT DOCUMENTATION PAGE			*Form Approved OMB No. 0704-0188*

1. AGENCY USE ONLY ***(Leave blank)***	**2. REPORT DATE** September 2018	**3. REPORT TYPE AND DATES COVERED** Master's thesis

4. TITLE AND SUBTITLE MEMS UNDERWATER DIRECTION FINDING ACOUSTIC SENSOR	**5. FUNDING NUMBERS**
6. AUTHOR(S) German Eduardo Da Re	
7. PERFORMING ORGANIZATION NAME(S) AND ADDRESS(ES) Naval Postgraduate School Monterey, CA 93943-5000	**8. PERFORMING ORGANIZATION REPORT NUMBER**
9. SPONSORING / MONITORING AGENCY NAME(S) AND ADDRESS(ES) N/A	**10. SPONSORING / MONITORING AGENCY REPORT NUMBER**

11. SUPPLEMENTARY NOTES The views expressed in this thesis are those of the author and do not reflect the official policy or position of the Department of Defense or the U.S. Government.

12a. DISTRIBUTION / AVAILABILITY STATEMENT Approved for public release. Distribution is unlimited.	**12b. DISTRIBUTION CODE** A

13. ABSTRACT (maximum 200 words)

Acoustic sensors operating in underwater environments were designed and fabricated based on the ear structure of the parasitic fly, *Ormia ochracea*. The design was executed using COMSOL Multiphysics, including mass loading and viscous damping. The optimized sensors were fabricated using MEMSCAP commercial foundry service. The testing was performed using NPS water tanks and TRANSDEC's San Diego underwater testing facility. For underwater characterization, a custom housing was made to immerse the sensors in a non-conducting fluid with acoustic impedance close to water. Measurements showed that the sensors could detect underwater sound with a narrow-band spectral response. Directional response of the sensors showed the expected cosine dependence, indicating their ability to detect the bearing of underwater sound sources. The sensor enclosure affected the measurements due to its non-uniform response to the incident sound. A reference hydrophone was similarly enclosed and COMSOL simulations performed to reduce and understand this effect. The results show that the enclosure produces unwanted resonance frequencies. For uniquely determining sound-source bearing, it is necessary to use two sensors at a canted angle. The circuit boards affected directional responses. COMSOL simulations were performed with actual-sized circuit boards. Several approaches to determine the optimal angle based on these observations are presented in this thesis.

14. SUBJECT TERMS MEMS, direction finding, *Ormia ochracea*, underwater, acoustic sensor	**15. NUMBER OF PAGES** 85
	16. PRICE CODE

17. SECURITY CLASSIFICATION OF REPORT	**18. SECURITY CLASSIFICATION OF THIS PAGE**	**19. SECURITY CLASSIFICATION OF ABSTRACT**	**20. LIMITATION OF ABSTRACT**
Unclassified	Unclassified	Unclassified	UU

NSN 7540-01-280-5500 Standard Form 298 (Rev. 2-89) Prescribed by ANSI Std. 239-18

THIS PAGE INTENTIONALLY LEFT BLANK

Approved for public release. Distribution is unlimited.

MEMS UNDERWATER DIRECTION FINDING ACOUSTIC SENSOR

German Eduardo Da Re
Lieutenant Commander, Argentina Navy
Electrical Engineer, Universidad de Mendoza, 1999

Submitted in partial fulfillment of the
requirements for the degree of

MASTER OF SCIENCE IN ENGINEERING ACOUSTICS

from the

NAVAL POSTGRADUATE SCHOOL
September 2018

Approved by: Gamani Karunasiri
Advisor

Fabio D. Alves
Co-Advisor

Oleg A. Godin
Chair, Engineering Acoustics Academic Committee

THIS PAGE INTENTIONALLY LEFT BLANK

ABSTRACT

Acoustic sensors operating in underwater environments were designed and fabricated based on the ear structure of the parasitic fly, *Ormia ochracea*. The design was executed using COMSOL Multiphysics, including mass loading and viscous damping. The optimized sensors were fabricated using MEMSCAP commercial foundry service. The testing was performed using NPS water tanks and TRANSDEC's San Diego underwater testing facility. For underwater characterization, a custom housing was made to immerse the sensors in a non-conducting fluid with acoustic impedance close to water. Measurements showed that the sensors could detect underwater sound with a narrow-band spectral response. Directional response of the sensors showed the expected cosine dependence, indicating their ability to detect the bearing of underwater sound sources. The sensor enclosure affected the measurements due to its non-uniform response to the incident sound. A reference hydrophone was similarly enclosed and COMSOL simulations performed to reduce and understand this effect. The results show that the enclosure produces unwanted resonance frequencies. For uniquely determining sound-source bearing, it is necessary to use two sensors at a canted angle. The circuit boards affected directional responses. COMSOL simulations were performed with actual-sized circuit boards. Several approaches to determine the optimal angle based on these observations are presented in this thesis.

THIS PAGE INTENTIONALLY LEFT BLANK

TABLE OF CONTENTS

LIST OF FIGURES

LIST OF TABLES

THIS PAGE INTENTIONALLY LEFT BLANK

LIST OF ACRONYMS AND ABBREVIATIONS

DF	Direction finding
FEM	Finite element modeling
ILD	Inter-aural level difference
ITD	Inter-aural time difference
MEMS	Micro electrical mechanical systems
NPS	Naval Postgraduate School
PA	Pressure acoustic
PCBs	Printed circuit boards
SEM	Scanning electron microscope
SM	Solid mechanics
SOIMUMPS	Silicon-on-insulator multi-user manufacturing process
TA	Thermoviscous acoustic
UW	Underwater

THIS PAGE INTENTIONALLY LEFT BLANK

ACKNOWLEDGMENTS

I want to thank the Sensor Research Lab members for allowing me to be a part of this amazing group. My predecessors, Swan and Collins, who led this innovative line of research using a sensor based on the fly's ears in an underwater environment, motivated me to join this team.

My advisors, Dr. Gamani Karunasiri and Dr. Fabio Alves, gave me confidence, knowledge, and support. There are not enough words to describe how your mentoring helped me to develop critical thinking and start along the scientist’s path. More importantly, you increased my satisfaction at being a part of this amazing team. Thank you.

To the professors and staff of the Physics Department—Dr. Bruce Denardo, Dr. Oleg Godin, Dr. Peter Crooker, Prof. Raymond Gamache, Jeff Catterlin, Steven Jacob, and Jay Adeff—thank you for your support and knowledge. I am also grateful to my partners in the lab, Alberto Espinoza, Jaehyun Park, Leroy Pimental, and Parminder Riarh, who shared their experiences and friendship.

Finally, to my beautiful wife, Valeria, and children, Antonella and Lourdes, thank you for your support, sacrifice, and love. They have allowed us to enjoy this journey in Monterey, California.

THIS PAGE INTENTIONALLY LEFT BLANK

I. INTRODUCTION

A sensor is a device that detects changes of its environment and generates a signal with specific information. For applications involving acoustics, sensors can be used to measure, for example, sound pressure, frequency, and particle velocity, among others. A sound wave can produce changes in pressure, temperature, and particle velocity as it propagates in a medium. Using some of these parameters, the direction of the arrival of a sound wave can be extracted, which can be used for localizing sound sources. This problem has been considered numerous times and different techniques were employed to accurately determine the direction of arrival. One approach to solve this problem is to study nature and see how it was solved. The type of sensors used in this approach are commonly known as bio-inspired. A bio-inspired directional sound sensor operating in air was developed previously based on the ear structure of the parasitic fly, *Ormia Ochracea,* at the Sensor Research Lab (SRL) in the Naval Postgraduate School (NPS). The success of this research motivated us to extend the effort to develop a directional acoustic sensor for underwater (UW) applications, which is described in this thesis.

A. BACKGROUND

1. Directional Sensing

A physicist, J. B. Venturi, stated in 1796 that when it comes to human hearing, "the inequality of the two impressions, which are perceived at the same time by both ears, determines the correct direction of the sound." The British physicist Lord Rayleigh confirmed this later and concluded that the binaural system direction finding (DF) capability is based on interaural time (ITD) and intensity level differences (ILD) [1].

To determine the direction of an acoustic source, both ears need to be excited by the incoming sound pressure field. Humans use this principle to determine the direction of the source with an accuracy of less than 2 degrees [2]. The ability to process the DF is related to the ears' separation compared to the wavelength of sound involved. In relatively large animals this distance is generally larger than the acoustic wavelength, meaning ITD and ILD are large enough to be detectable by the central nervous system. In smaller

animals, the ITD and ILD can be extremely small, which reduces the directional accuracy. Many smaller animals have developed mechanisms for effectively increasing ITD and ILD before they are processed by the central nervous system [3].

Among the different approaches, *Ormia ochracea* employs a unique approach to DF. Using her direction-sensing ears, the female fly locates crickets via their mating calls, and lays her eggs over the host. The cricket's mating call exhibits a chirp around 4.8 kHz, corresponding to a wavelength of about 7 cm. The entire hearing organ of the fly is about 1.5 mm, giving a substantial wavelength mismatch. Unlike most ears, according to [3], the fly's ears "are not physically separated but are contained within a common air-filled chamber" and mechanically coupled, "450 to 520 microns apart from each other," as shown in Figure 1. This mechanical coupling between the ears increases the ITD by a factor of about 20 [3].

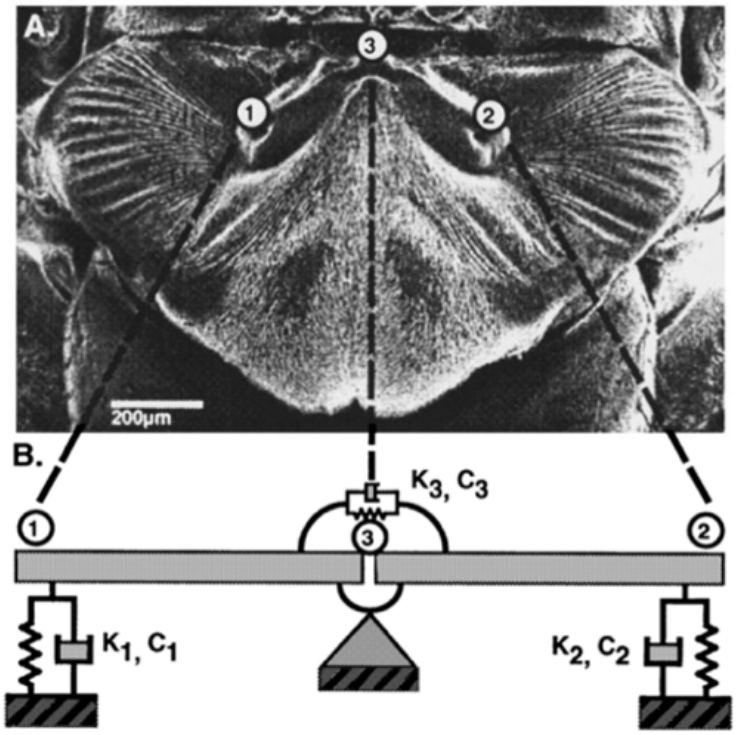

Figure 1. *Ormia ochracea* fly's hearing organ and its mechanical equivalent. Source: [3].

In effect, the mechanical system expands ILD and ITD. According to Miles et al. [3], "the motion is decomposed into two 'natural' modes of vibration." The first consists of both ends moving out of phase, or pure "rocking." The second consists of both ends moving in phase with equal amplitude or "bending." The rocking responds only to the difference between the forces while the bending only to the sum of the forces, as shown in Figure 2 [3].

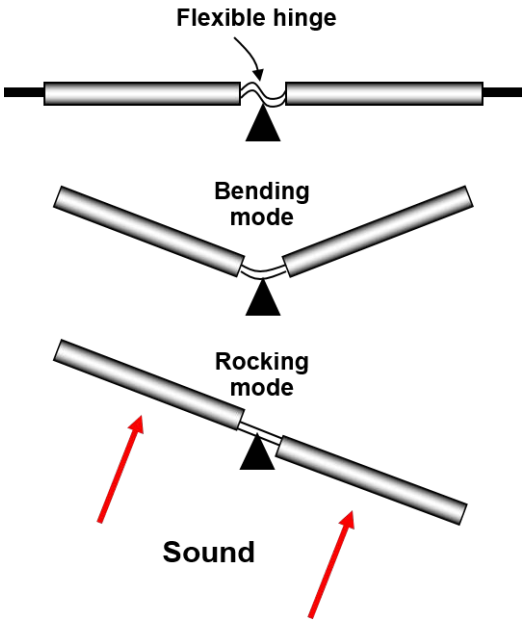

Figure 2. Vibration modes of *Ormia ochracea* hearing system. Source: [4].

Numerous micro-electro-mechanical-system (MEMS)-based devices have been designed based on the operation principle of *Ormia ochracea's* hearing system [5]. These sensors exhibit narrow spectral responses, and transduction is achieved using optical [6], piezoelectric [7], or capacitive [8] means.

2. MEMS Sensor Designs

The development of *Ormia*-based MEMS sensors has been an important task in the Sensor Research Lab at NPS. Since 2006, several different versions of directional sensors

were developed to primarily operate in air. The common feature of these sensors was the sensing of vibration of the mechanical structure using comb finger capacitors.

Details on the design, fabrication, and characterization procedure are well documented in Touse's [9] and Downey's [10] PhD dissertations and in many other master's theses at NPS.

Figure 3 shows one of the first MEMS sensors employing comb finger capacitor readout system. This design includes a solid bridge that connects two wings of the sensor and the entire mechanical system is connected to the substrate using two torsional legs. The capacitive comb's fingers attach to the end of the wings and overlap with the fixed comb's fingers attached to the substrate. This configuration allows for the capacitance of the combs' fingers to vary proportionally to the displacement of wings under sound excitation. Therefore, the acoustic pressure on the wings transforms the mechanical motion into an electrical signal, proportional to the movement of the wings, emulating the hearing system of the fly [8]. The change of this capacitance is read out by using a MS3110 Universal Capacitive Readout IC from Irvine Sensors Corporation in California [11].

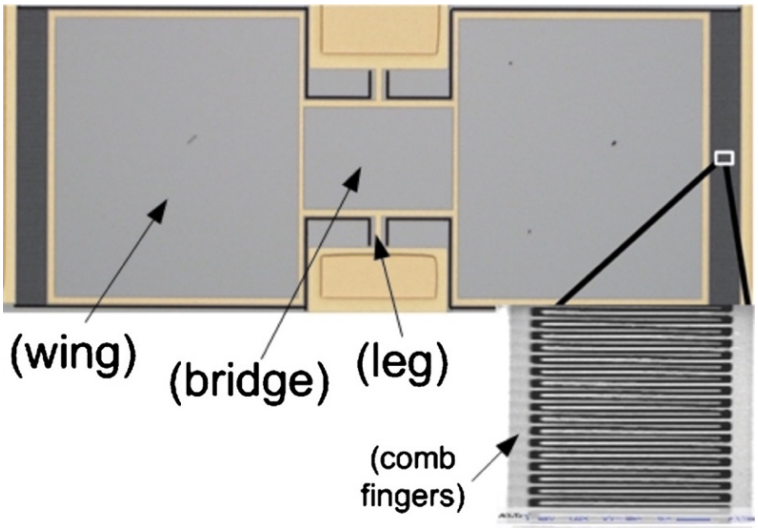

Figure 3. Previous generation of MEMS sound sensor with integrated comb finger capacitors. Source: [8].

All the sensors were fabricated by MEMSCAP Inc. foundry service through the Silicon-on-Insulator Multi User MEMS Process (SOIMUMPS) [8].

When the sensor was operated with both front and back sides exposed to sound, the bending mode produced the predominant vibration amplitude. It showed a cosine dependence with respect to the incident direction of sound, making the sensor act like a pressure-gradient microphone, as shown in Figure 4 [4]. The previous generation of sensors were primarily developed for operating in air. It is possible to design similar sensors for operating in UW environments, however.

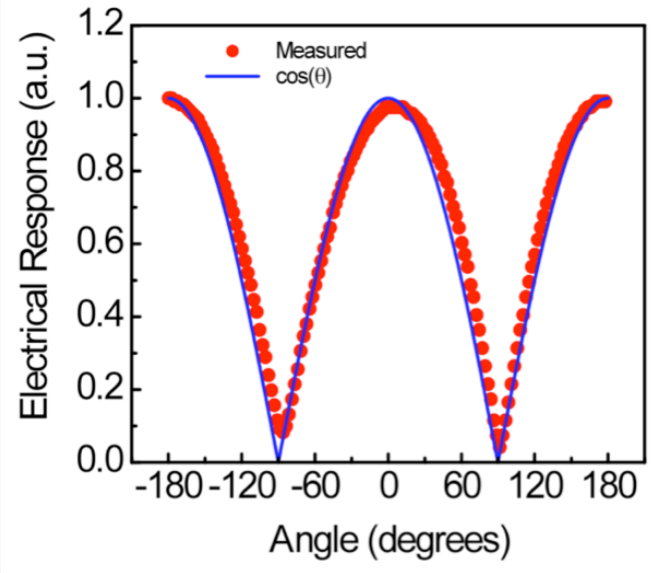

Figure 4. Cosine dependence on the angle of incidence. Source: [11].

B. UNDERWATER MEMS DIRECTIONAL FINDING

Swan [12] presented the first design for an UW single-wing MEMS sensor as shown in Figure 5. To operate the sensor in UW, it needs to be placed in an acoustically transparent housing for the wavelength of interest and filled with a fluid having acoustic impedance close to that of water. In addition, it should not be conducting and have low viscosity to allow the combs' finger capacitors to work properly. In the initial sensor design, gap between the combs' fingers was increased from 2 μm (used for operating in air) to reduce the damping due to higher viscosity of the liquid. The sensors were designed

with 5- and 10-μm comb finger gap sizes, to investigate the performance of the sensors against the dumping caused by the interaction of fluid and combs' fingers.

For the sensor housing, a three-millimeter urethane Flexane 80 boot was designed with a sound speed of $c = 2400 \pm 25\ m/sec$ and density $\rho = 1045\ kg/m^3$, giving an acoustic impedance of $r = \rho \times c = 2.51 \times 10^6 Pa.s/m$. The fluid selected for the housing was PSF-2cSt silicon fluid whose acoustic impedance was $r_{oil} = 9.41 \times 10^5 Pa \cdot s/m$, giving a transmission coefficient $T = 0.95$ [12].

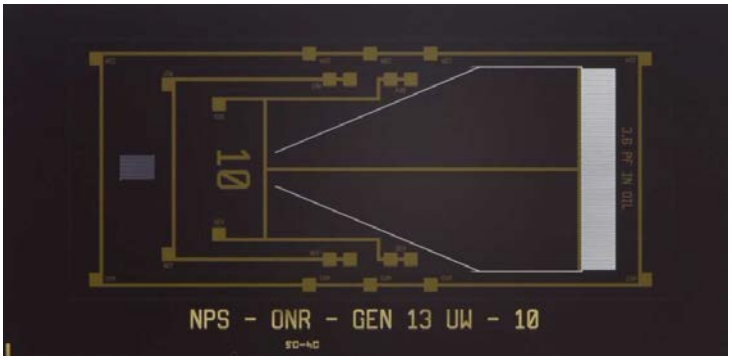

Figure 5. Gen 1 underwater MEMS sensor. Source: [13].

Subsequently, Collins [13] studied how the frequency characteristics are affected by variation of the thickness of the layer used for the mechanical structure of the sensor. This uncertainty of thickness (± 1μm) can make the sensor thickness vary between 24–26 microns, which changes the mass of the wings and hence the resonance frequency. Collins also examined the damping effects as well as drag forces on the wings and the comb finger capacitors, which are important in determining the frequency response and quality factor [13]. In addition, the residual stress on the wings generated during the fabrication process was also probed using the models developed in [10]. The residual stress causes the wing to bend, which reduces the overlap between moving and fixed combs. This significantly reduces the comb finger capacitance, which lowers the sensitivity [10], [13]. To overcome this limitation, a sensor with shorter wings was designed (Figure 6).

The sensor has not been fully characterized due to NPS's water tank limitations; initial measurements on the sensor showed it was able to detect UW sound, however.

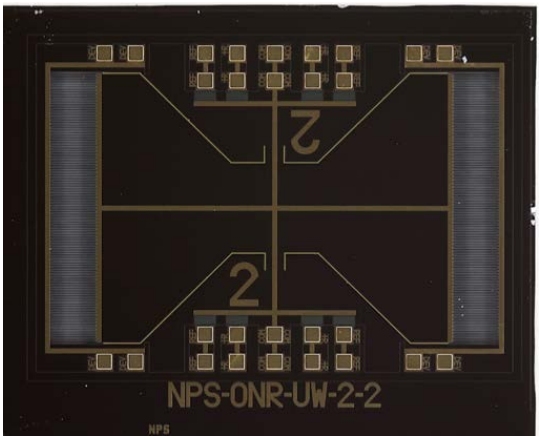

Figure 6. Gen 2 MEMS with two shorter wings. Source: [13].

C. PURPOSE AND THESIS STRUCTURE

This thesis is a continuation of the study of *Ormia*-based acoustic directional sensors for UW applications. Therefore, an extensive study on effects of viscous losses, housings, and sensors assemblies to mitigate directional ambiguity was performed. Due to the sensor's interaction with surrounding fluid, the problem becomes more complex due to the small dimensions of the sensor as well as requiring it be in fluid when it is immersed.

This thesis is organized in six chapters: Chapter I summarizes previous work on MEMS directional sound sensors as well as the initial work on exploring sensors operating in UW environments.

Chapter II describes viscous loss effects in MEMS sensors. Finite element modeling (FEM) with COMSOL Multiphysics software was used to simulate these effects and compare with measurements. Thermoviscous acoustic (TA) and pressure acoustic (PA) physics was employed to achieve a realistic model to describe the fluid structure interactions. Recent measurements show that this effect plays an important role in the frequency response of the sensor.

Chapter III presents results of the UW sensor characterization in the Acoustic Transducer Evaluation Center (TRANSDEC), a facility that belongs to Space and Naval Warfare Systems Command (SPAWAR) in San Diego.

Chapter IV presents the effects housing (boot) used for enclosing the sensor and its performance. The materials and dimensions of the boot were found to affect the sensor's frequency response, which alters its intrinsic characteristics. This effect was observed experimentally, and COMSOL Multiphysics model was developed to understand how to minimize it.

Chapter V explores the canted angle assembly needed for unambiguous determination of direction since each sensor gives symmetric response off normal incidence. This approach uses two sensors placed at a canted angle to uniquely determine the direction. This study was conducted in air before implementing it in an UW environment in the future.

Chapter VI presents the conclusion of this thesis and suggestions for future work.

II. MEMS SENSOR WITH THERMOVISCOUS LOSSES

A. BACKGROUND

Compression and expansion in a fluid produce acoustic waves. If these changes are small, the acoustic waves are in the linear regime and the process can be considered adiabatic and reversible [14]. Thermal and viscous losses are important factors when the acoustic wave interacts with MEMS sensors, however, causing attenuation of the vibration amplitude and broadening of the resonance peak [15]. In addition to the damping effects, the mass loading can shift the resonant peak to lower frequency. In order to model sensor characteristics accurately, the geometry, the material selection, and the physics are critical for the final result.

COMSOL Multiphysics is used to model MEMS sensor performance when immersed in a fluid. It is a simulation software that computes coupled physical phenomena through finite element analysis (FEA). The physical models are discretized and processed by finite element method (FEM) to generate the desired characteristics. The math behind this process involves solving of relevant partial differential equations (PDEs) associated with the physics involved [15].

B. MEMS SENSOR DESIGN

The first UW sensor (Gen1) was a single-wing sensor (see Figure 7) with 5- and 10-micron comb finger gaps. To model the sensor in COMSOL, the first step is to design its geometry. Two types of geometry were designed for the simulation: with and without comb fingers. For the design without comb fingers, their effects were included in the simulation by using appropriate parameters and equations to take into account the damping effects. This approach provides faster simulation due to the reduction of meshing nodes associated with a large number of combs. The sensor has only one fixed constraint at the pivot point, as shown in Figure 7.

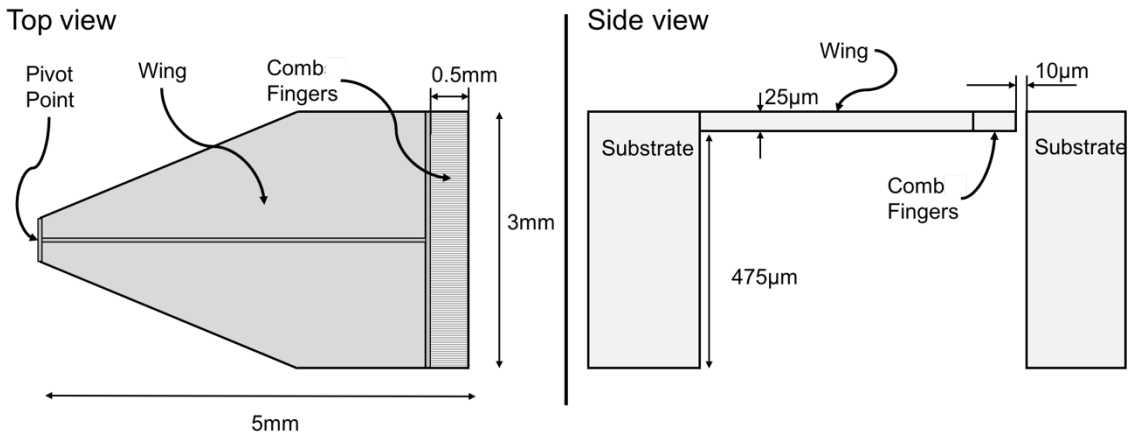

Figure 7. Schematic top view and side view of the single-wing underwater sensor.

C. MATERIAL PARAMETERS

The selection and characteristic of the materials used in fabrication of sensors are critical to building an accurate model. The mechanical structure of the sensor is constructed using silicon, which is an anisotropic material. Therefore, its Young's modulus depends on the orientation relative to the crystal lattice. Its value can vary up to 45%, from 130 to 188 GPa, producing significant influence on the simulation results [16].

Hook's law describes how stress (σ) and strain (ε) relate in terms of compliance (S) or stiffness (C) [16].

$$\sigma = C\varepsilon \quad \varepsilon = S\sigma \tag{2.1}$$

For anisotropic material, this relationship is described by a fourth-rank tensor with 81 terms. The cubic symmetry of the silicon reduces it to three independent components and can be written in a matrix format (see Equations 2.2 and 2.3), where the values for each entry came from the Young's modulus (E), Poisson ratio (ν), and the shear modulus (G) [16].

$$\begin{bmatrix}\sigma_{xx}\\ \sigma_{yy}\\ \sigma_{zz}\\ \sigma_{yz}\\ \sigma_{zx}\\ \sigma_{xy}\end{bmatrix} = \begin{bmatrix} \frac{1-\nu_{yz}\nu_{zy}}{E_yE_z\Delta} & \frac{\nu_{yx}+\nu_{yz}\nu_{zy}}{E_yE_z\Delta} & \frac{\nu_{zx}+\nu_{yz}\nu_{zy}}{E_yE_z\Delta} & 0 & 0 & 0 \\ \frac{\nu_{xy}+\nu_{xz}\nu_{zy}}{E_zE_x\Delta} & \frac{1-\nu_{zx}\nu_{xz}}{E_zE_x\Delta} & \frac{\nu_{zy}+\nu_{zx}\nu_{xy}}{E_yE_z\Delta} & 0 & 0 & 0 \\ \frac{\nu_{xz}+\nu_{xy}\nu_{yz}}{E_xE_y\Delta} & \frac{\nu_{yz}+\nu_{xz}\nu_{yx}}{E_xE_y\Delta} & \frac{1-\nu_{xy}\nu_{yx}}{E_xE_y\Delta} & 0 & 0 & 0 \\ 0 & 0 & 0 & G_{yz} & 0 & 0 \\ 0 & 0 & 0 & 0 & G_{zx} & 0 \\ 0 & 0 & 0 & 0 & 0 & G_{xy} \end{bmatrix} \cdot \begin{bmatrix}\varepsilon_{xx}\\ \varepsilon_{yy}\\ \varepsilon_{zz}\\ \varepsilon_{yz}\\ \varepsilon_{zx}\\ \varepsilon_{xy}\end{bmatrix} \qquad (2.2)$$

$$\Delta = \frac{1-\nu_{xy}\nu_{yx}-\nu_{yz}\nu_{zy}-\nu_{zx}\nu_{xz}-2\nu_{xy}\nu_{yz}\nu_{zx}}{E_xE_yE_z} \qquad (2.3)$$

The MEMS devices are typically fabricated using (100) oriented silicon wafers with principle axes along [110], [1$\bar{1}$0], and [001] directions [16]. The elasticity parameters corresponding to these directions are in Equations (2.4) and (2.5), which generate the stiffness matrix as given in Equation (2.6). These values are later inserted in the material elasticity matrix in COMSOL.

$$E_x = E_y = 169\ GPa \quad E_z = 130\ GPa \qquad (2.4)$$

$$\nu_{yz} = 0.36\ \nu_{zx} = 0.28\ \nu_{xy} = 0.064 \qquad (2.5)$$

$$\begin{bmatrix}\sigma_1\\ \sigma_2\\ \sigma_3\\ \sigma_4\\ \sigma_5\\ \sigma_6\end{bmatrix} = \begin{bmatrix} 194.5 & 35.7 & 64.1 & 0 & 0 & 0 \\ 35.7 & 194.5 & 64.1 & 0 & 0 & 0 \\ 64.1 & 64.1 & 165.7 & 0 & 0 & 0 \\ 0 & 0 & 0 & 79.6 & 0 & 0 \\ 0 & 0 & 0 & 0 & 79.6 & 0 \\ 0 & 0 & 0 & 0 & 0 & 50.9 \end{bmatrix} \cdot \begin{bmatrix}\varepsilon_1\\ \varepsilon_2\\ \varepsilon_3\\ \varepsilon_4\\ \varepsilon_5\\ \varepsilon_6\end{bmatrix} in\ GPa \qquad (2.6)$$

D. PHYSICS EMPLOYED IN MODELING

To improve the UW MEMS sensor model, thermal conduction and viscous losses are incorporated using the Thermoviscous Module in COMSOL. This module employs a linearized Navier-Stokes equation [15].

The Navier-Stokes equation governs the motion of fluid and can be seen as Newton's second law of motion for fluids [15].

Viscosity and thermal conduction effects dissipate energy near the boundary of the structure within the acoustic boundary layer, producing losses that affect the sensor characteristics.

The governing equations are derived by adopting small harmonic oscillations and can be described using

$$p = p_0 + p'\, e^{i\omega t},\ u = u_0 + u' e^{i\omega t},\quad T = T_0 + T' e^{i\omega t}, \tag{2.9}$$

where p is the acoustic pressure, u is the acoustic velocity (particle velocity), T is the acoustic temperature variations, and ω is the angular frequency. If the fluid is stationary, then the average fluid velocity, $\vec{u}_0 = 0$. Introducing these conditions into the governing equations and only retaining the first-order linear terms yield the wave equation including thermal and viscous effects [15].

The continuity equation is

$$i\omega\rho = -\rho_0(\nabla \cdot \vec{u}), \tag{2.10}$$

where ρ_0 is the background density and ω is angular frequency.

The momentum equation is

$$i\omega\rho_0 u = \nabla \cdot \left(-pI + \mu(\nabla u + (\nabla u)^T) + \left(\mu_B - \frac{2}{3}\mu\right)(\nabla \cdot u)I\right), \tag{2.11}$$

where μ is the dynamic viscosity, $\mu_B$is the bulk viscosity and the right-hand side represents the divergence of the stress tensor, I is the identity matrix, and T superscript denotes transposed matrix operation [15].

The energy conservation equation is

$$i\omega\left(\rho_0 C_p T - T_0 \alpha p\right) = -\nabla \cdot (-k\nabla T) + Q, \tag{2.12}$$

where C_p is the heat capacity at constant pressure, k is the thermal conductivity, α_0 is the coefficient of thermal expansion, and Q is any possible source of heat [15].

The linearized equation of state relates pressure, temperature, and density and is given by

$$\rho = \rho_0(\beta_T p - \alpha_0 T), \tag{2.13}$$

where β_T is the isothermal compressibility.

The length scale is given by the thickness of the viscous boundary layer, which is

$$\delta_v = \sqrt{2\mu/(\omega\rho)}, \tag{2.14}$$

and the thickness of the thermal boundary layer [15] is

$$\delta_t = \sqrt{2k/(\omega\rho_0 C_p)}\,. \tag{2.15}$$

These parameters are relevant during the meshing to take into account viscous and thermal effects. The preserved quantities, mass, momentum, and energy are on the left-hand side of the governing equations. The right-hand side represents the process that locally changes or modifies the preserved quantity. Diffuse loss terms due to viscous and thermal conduction are present in two equations. Gradients in the velocity field reveal viscous losses while gradients in the temperature reveal thermal losses [15].

The baseline model was designed with two coupled physics, PA and solid mechanics (SM) domains. To include the thermal and viscous losses, the TA module is added. TA physics increases the computational time because of the number of equations that the software has to solve, as well as the number of degrees of freedom due to the mesh needed for that physics. Therefore, a small boundary is set up around the sensor, where it is relevant and coupled with the PA physics, as illustrated in Figure 8 [15].

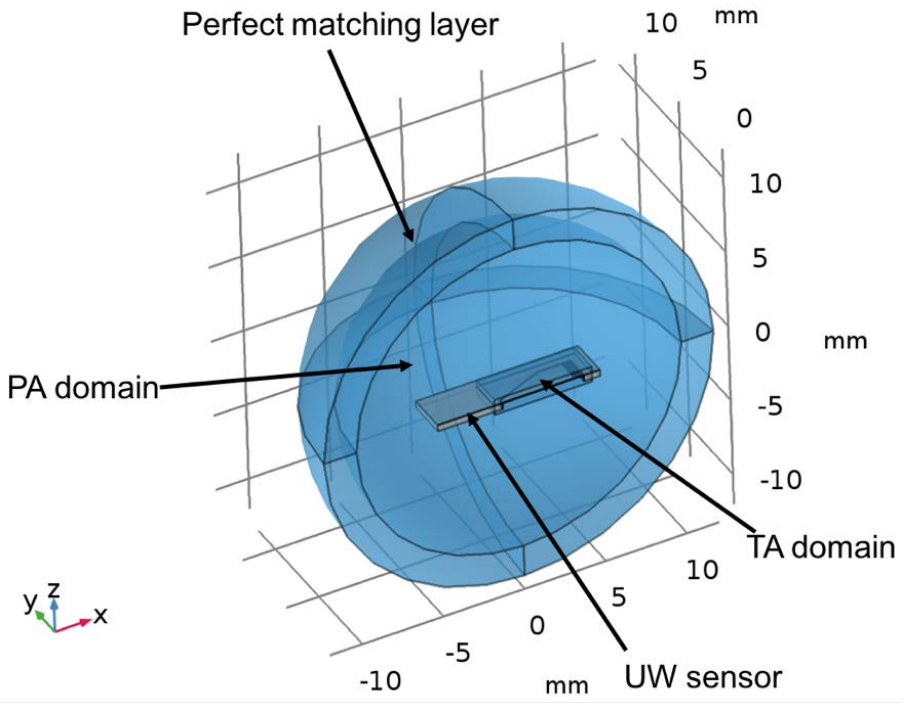

The outer spherical shell represents a perfectly matched layer (PML) that plays the role of an anechoic layer; the inner sphere is assigned with the PA domain where the incident plane wave originates. The sensor is surrounded by the TA domain, which is coupled to the PA domain.

Figure 8. Schematics of COMSOL model showing different physics.

E. SIMULATION

Two different studies were performed using the model Gen1 sensor in the frequency domain. The first study was a frequency sweep with three different sensor and physics configurations. The second study was a parametric thickness sweep to probe how it affects the resonant peak position. The entire simulation volume was filled with silicone oil with density 818 Kg/m^3 and viscosity of 1 cSt.

1. Gen1-10 Sensor Simulation

In this study, three different simulations were carried out to compare the frequency responses between PA and TA modules, and how the actual geometry of the comb fingers affects the frequency response when they are added to the model. The symmetry of the sensor geometry allowed us to carry out the computation using half of the sensor using symmetry boundary condition feature in COMSOL to reduce the computation time.

The first simulation was a simplified model of the sensor without comb fingers and using only PA physics, as shown in Figure 9-A. To compute the comb's effect, density of the comb section was reduced and a boundary load was applied to generate the expected damping from the comb [13]. In the second simulation, the TA physics is added to the simplified model, as shown in Figure 9-B. In the third simulation, actual combs were incorporated in the design (see Figure 9-D) and modeled with the TA physics, as shown in Figures 9-C and 9-D.

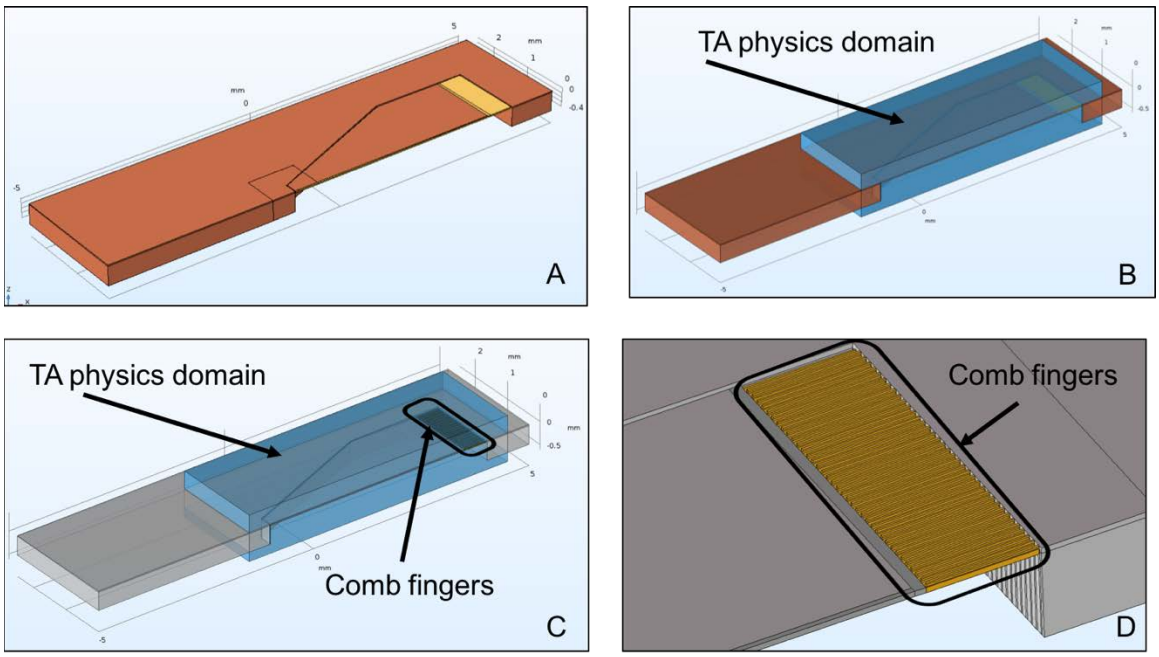

Figure 9-A shows the sensor without combs embedded in PA physics. Figure 9-B shows the sensor without combs including TA physics. Figure 9-C shows the sensor with TA physics and actual comb fingers. Figure 9-D shows the details of the comb fingers.

Figure 9. Gen1-10 Sensor COMSOL models.

To generate the frequency response of the sensor, the displacement of the tip of the sensor wing was computed using a 45º incoming plane wave. The results are plotted using a Point Graph feature in COMSOL. This study allows us to compare how different physics affect the frequency response.

Figure 10 shows frequency responses for the three different models shown in Figure 9. This sensor when operated in air has resonant peak around 870 Hz [13]. The shift of the resonant peak to lower frequency when operated in fluid is primarily due to mass loading. When TA is incorporated in the simulation, the peak further shifts to the low frequency end and most likely due to accurate modeling of effect of fluid on the MEMS sensor. When actual combs were incorporated, the peak frequency was found to shift less than without combs. This may be due to the slight reduction of mass loading since the surface area of the sensor is slightly reduced compared to the entire comb area, which is covered with a uniform layer.

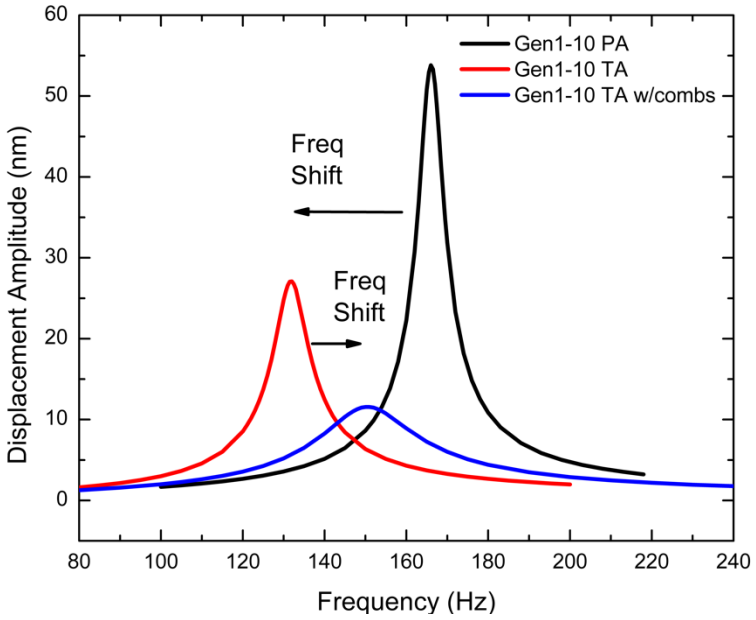

Simulated frequency responses for the three configurations in Figure 9. The sound source was a plane wave incident at 45 degrees off of the normal axis of the sensor. The sound pressure was 1 Pa.

Figure 10. Simulated frequency response of Gen1-10 sensor.

For comparison of the peak widths, data shown in Figure 10 was normalized as shown in Figure 11. The differences of peak widths are due to how different models take into account the viscous damping. The merits of different models can be assessed only after comparison with the experimental data, however. The thermal damping was found to be relatively small.

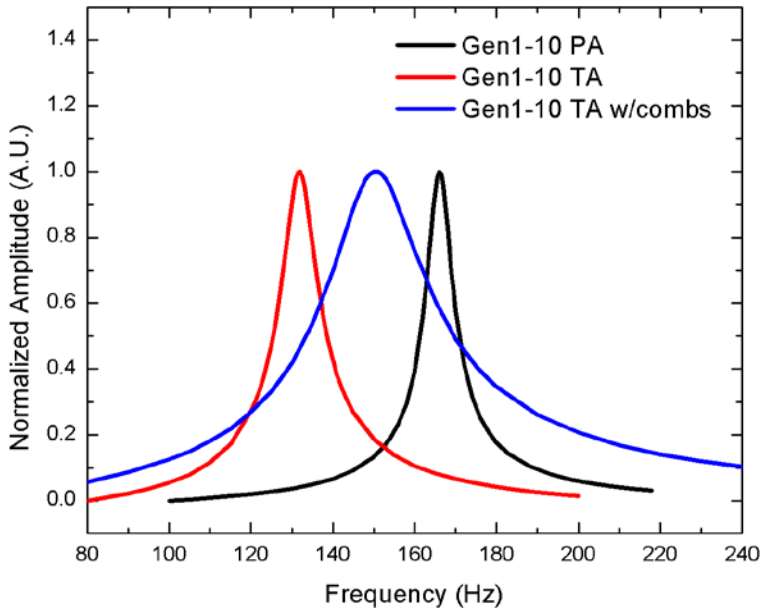

Figure 11. Normalized frequency responses for the Gen1-10 MEMS sensor.

2. Variation of Sensor Thickness

According to MEMSCAP, the device layer thickness of the silicon-on-insulator wafer used in the fabrication can vary from 24 to 26 μm [17]. To model how this variation affects the frequency response, a second study was made with a parametric sweep using the thickness as variable. The sensor model with actual combs and TA physics was used in this simulation. As expected, the simulation shows that the thickness affects frequency response, as shown in Figure 12. This frequency shift was found to be proportional to the thickness; every micron produces about 10 Hz frequency shift, as shown in Figure 12. This behavior can be explained qualitatively using the thickness (t) dependence of stiffness ($\propto t^3$) and mass of the wing ($\propto t$), which give the resonant frequency to vary as $(\text{stiffness/mass})^{1/2}$ or linear in t.

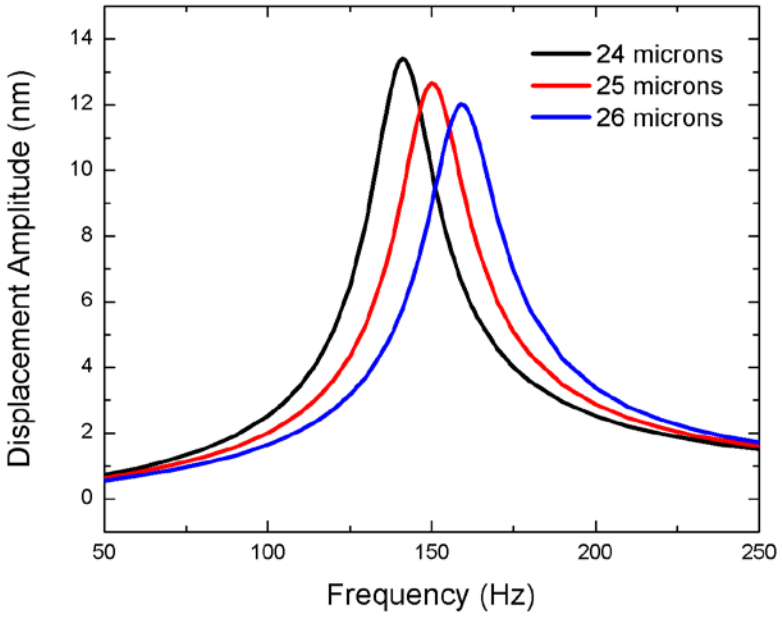

The figure shows the displacement of the resonance frequency due to the thickness uncertainty of the fabrication process.

Figure 12. Thickness parametric sweep.

III. GEN1-10 CHARACTERIZATION IN WATER

Due to low resonant frequency of the Gen1-10 sensor, a facility with relatively large water tank is required for characterization. The characterization involves both frequency and directional responses. The latter metric is important since it tells us about the sensor's ability of directional sensing in an UW environment.

A. TESTING FACILITY FOR UNDERWATER MEASUREMENT

The Acoustic Transducer Evaluation Center (TRANSDEC), a facility that belongs to Space and Naval Warfare Systems Command (SPAWAR) in San Diego, was selected to test the MEMS sensor. This center is a controlled environment with low ambient noise for transducer calibration. The pool has an eye-shaped perimeter and contains 6 million gallons of fresh water. Its dimensions are 300 ft. x 200 ft. x 38 ft. deep. According to [18], the reflection at the pool boundary is controlled and "the reflections from the walls and the air-water interface terminate in absorptive sound trap which surrounds the lip of the pool." With this technique, the interference of the reflected energy is highly reduced [18].

At the center of the pool, there is a bridge with a control room that houses all the electronic equipment, projectors, and calibrated hydrophones. This room is decoupled from the pool to minimize interference with measurements, as shown in Figure 13.

Figure 13. Aerial view of TRANSDEC pool. Source [19].

B. ASSEMBLY AND TESTING

A set of Gen1-10 sensors were assembled for testing. This included integration of readout electronics (MS3110 IC) to read vibration amplitude of wings under sound excitation. An assembled circuit board is depicted in Figure 14. The programming of MS3110 IC was carried out at the test site to make sure the sensor was working properly. All the equipment needed for data acquisition was shipped to the TRANSDEC facility prior to testing.

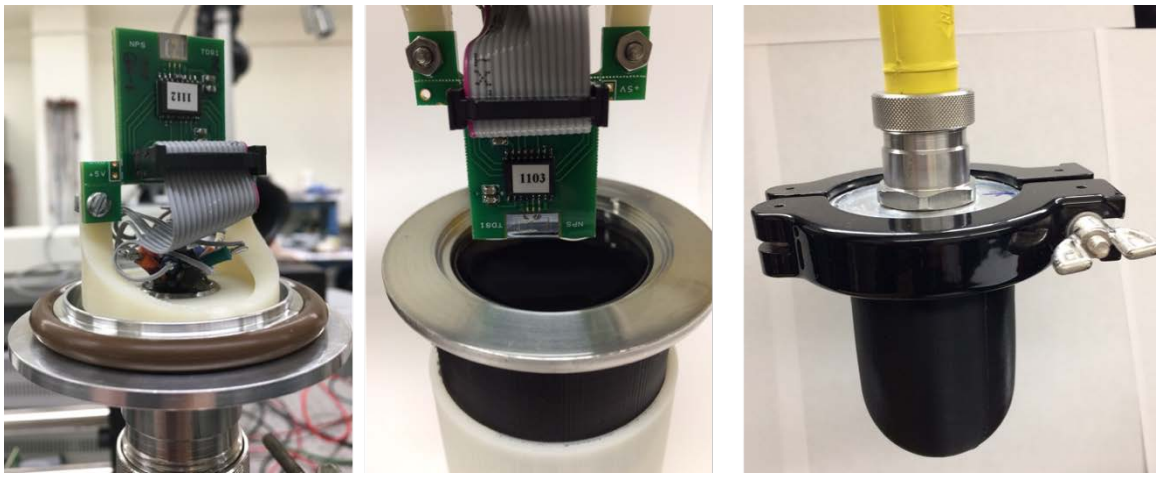

Figure 14. Assembled circuit board with Gen1-10 sensor.

The projector used for the measurement was a Lubell VC2C Underwater Acoustic Transducer (see Appendix B). For the measurement, two MFLI Zurich Lock-in amplifiers were used for simultaneously recoding signals from the sensor and reference hydrophone. The projector was excited using the master lock-in amplifier's internal reference signal via a power amplifier (see Figure 15). The B&K 8103 reference hydrophone and the MEMS sensor with identical boots were connected to the lock-in amplifiers as shown schematically in Figure 15. The output signal of the B&K 8103 hydrophones was amplified using a Stanford Research System low-noise preamplifier (SR560) before connecting to the lock-in amplifier. One of the lock-in amplifiers supplied +5 VDC through one of its outputs to the MEMS sensor. Both lock-in amplifiers were synchronized with a master-slave configuration. The results were monitored in real time using the computer interface to the lock-ins and the data are recorded in comma-separated values (CSV) files for post processing.

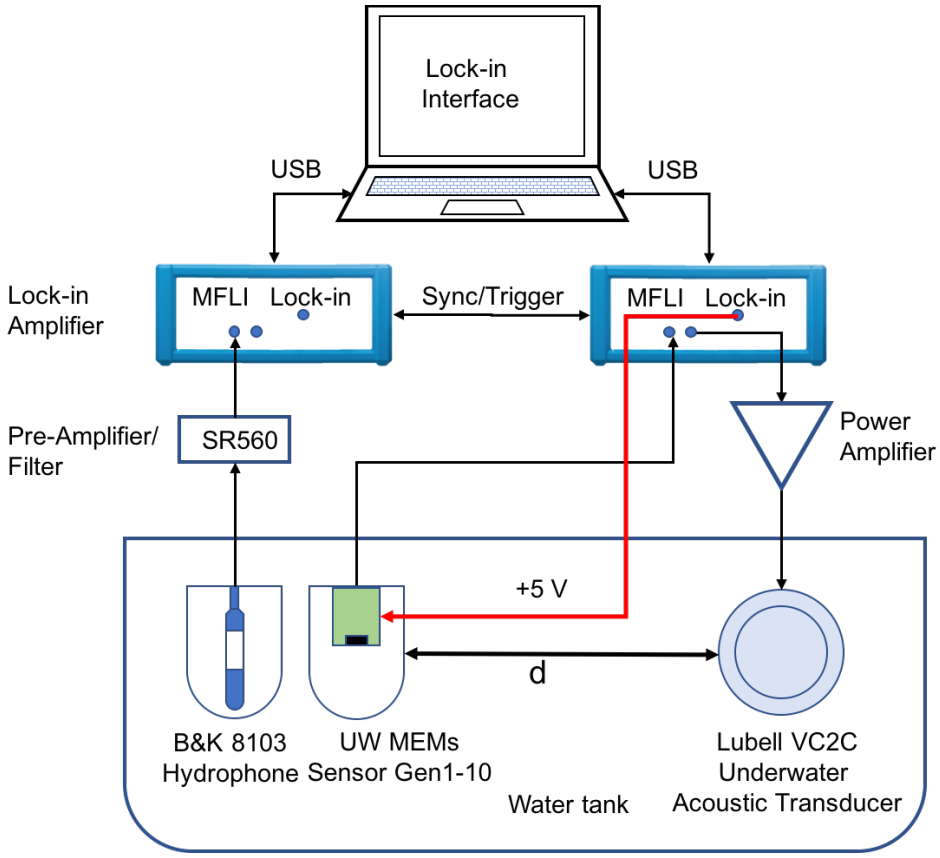

Figure 15. Schematic of data acquisition system.

C. RESULTS

1. Frequency Response

The frequency response measurement was performed from 50 to 400 Hz with 1 Hz steps. During the sweeping, the time constant is adjusted automatically by the lock-in amplifier, according to the sweeping frequency. Figure 16 shows the measured frequency response of the reference hydrophone (B&K 8103) with the boot attached to minimize the effects of the boot on the response.

The result of the reference hydrophone measurement shows how the projector's output varies with frequency. Note that, though the hydrophone has a flat frequency response (see Appendix A), the surrounding boot can alter it if the transmission of sound through it depends on frequency. It was found that a strong resonance of the source (around

110 Hz) is close to the sensor's resonant frequency, which can obscure the intrinsic sensor response.

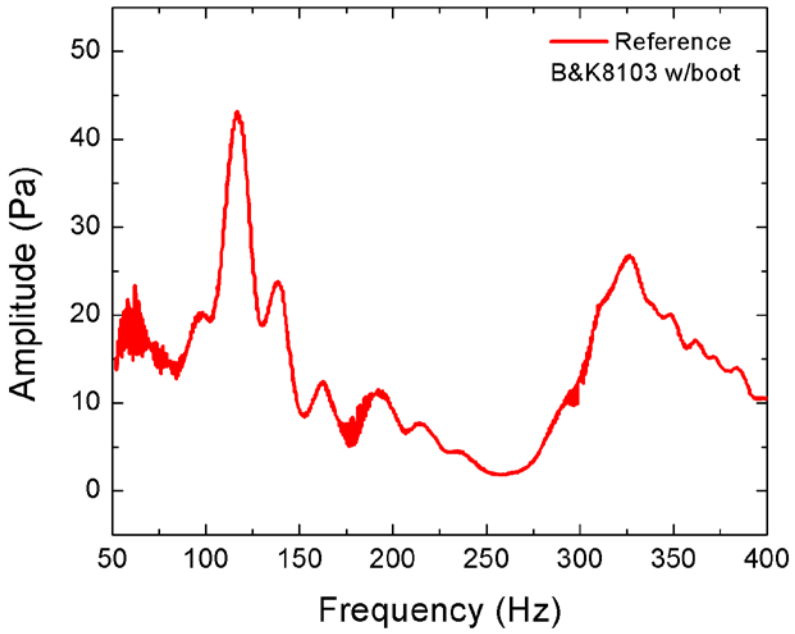

Figure 16. Frequency response of the reference hydrophone w/boot.

According to [14] the sensitivity for an open circuit is defined as

$$M = V/P, \tag{3.1}$$

where V is the output voltage and P is the pressure amplitude.

The sensitivity M of a hydrophone can be express in terms of its sensitivity level ML using [14]

$$ML\ (re\ M_{ref}) = 20\ log(M/M_{ref}\ ). \tag{3.2}$$

For the B&K Hydrophone (8130), the sensitivity level (see Appendix A) is

$$ML = -211.5\ dB\ re\ 1V/\mu Pa. \tag{3.3}$$

Using Equation (3.2), it is possible to determine M as follows

$$M = 10^{M_L/20} \cdot M_{ref} \xrightarrow{yields} M = 10^{\frac{-211.5}{20}} \cdot \frac{1V}{1\mu Pa} \cdot \frac{10^6 \mu Pa}{Pa}, \quad (3.4)$$

$$M = 26\mu V/Pa. \quad (3.5)$$

The sound pressure at the sensor can be obtained using the reference hydrophone signal V_R and gain of the SR560 preamplifier, G as

$$V_R = G \cdot M \cdot P \xrightarrow{yields} P = V_R/(G \cdot M). \quad (3.6)$$

Therefore, the sensitivity of the sensor, *Ms*, can be extracted using the measured signal *Vs* as

$$Ms = \frac{V_S}{P} \xrightarrow{yields} Ms = \frac{V_S}{V_R} \cdot G \cdot M. \quad (3.7)$$

Figure 17 shows the sensitivity of the Gen1-10 sensor extracted using (3.7) in V/Pa.

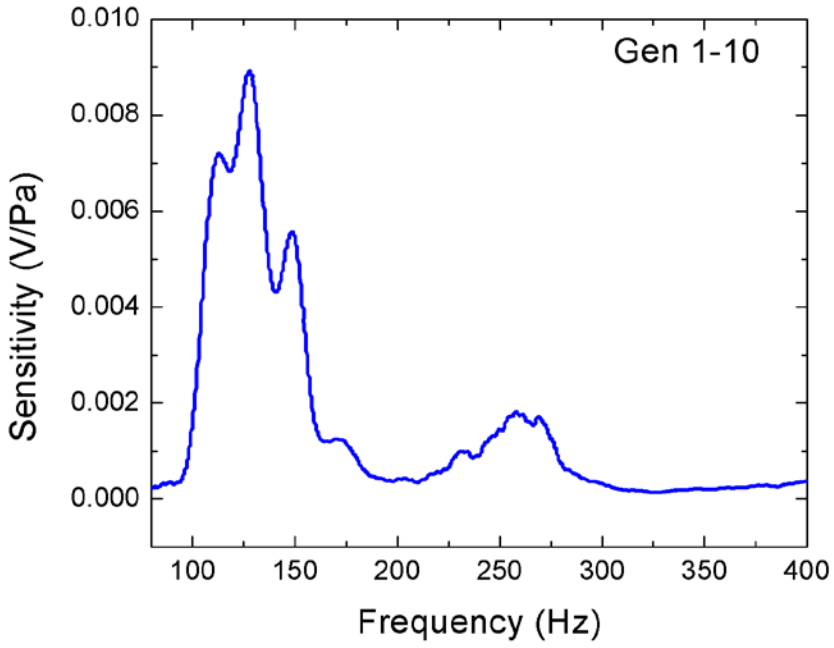

Measured sensitivity of Gen1-10 MEMS sensor at TRANSDEC.

Figure 17. Measured sensitivity of Gen1-10 sensor.

A comparison between the results of the measurement of the Gen1-10 at TRANSDEC and the COMSOL simulation (TA w/combs) gives reasonably good agreement, as shown in Figure 18. The effect from the boot and the resonance of the source can interfere with the measured sensitivity of the sensor, however, giving additional features in the plot.

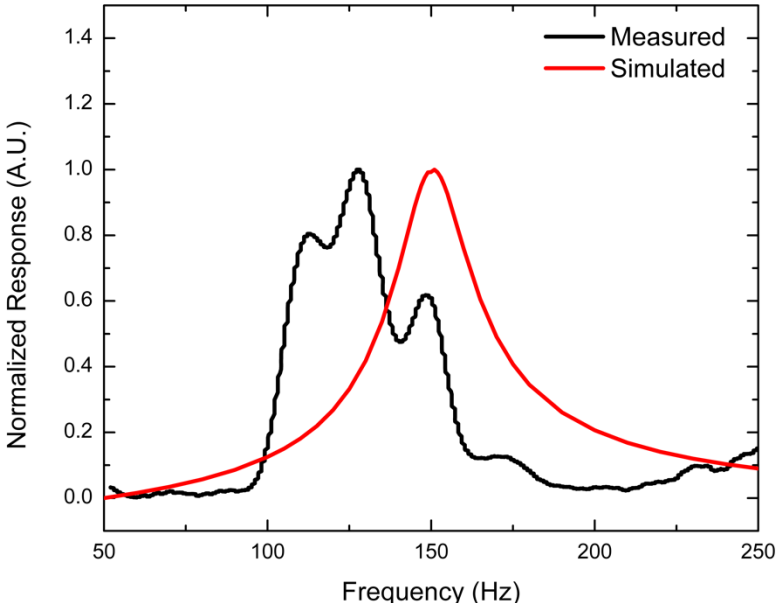

Comparison between measured and simulated data for Gen1-10 sensor. The two data sets were normalized since the simulation gives amplitude of oscillation in nm while measurement is the output signal in volts.

Figure 18. Comparison of measured and simulated data for Gen1-10 sensor.

2. Directivity Pattern

The directivity pattern of the sensor is one of the most important characteristics of an acoustic sensor. The directivity pattern shows how the sensitivity varies as function of direction. Most sensors are operated in the far-field range of the sound sources, which depends on wavelength and dimensions of the source. The distance to near-field/far-field boundary ($r_{\mathrm{NF/FF}}$) is also known as the Fraunhofer region and is given by [20]

$$r_{NF/FF} = \pi R_0^2/\lambda, \qquad (3.8)$$

where πR_0^2 is the cross-sectional area of the source, and λ is the wavelength, as shown in Figure 19.

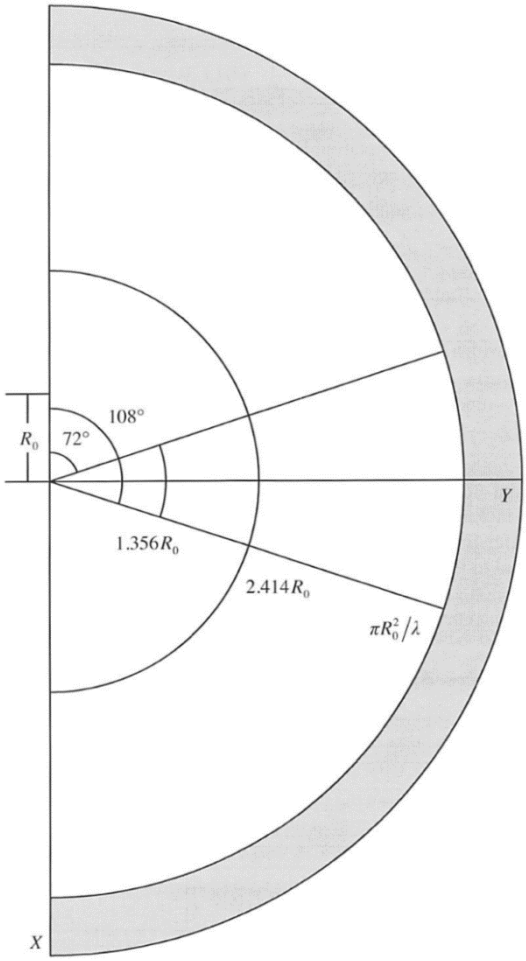

The region in gray indicates the Fraunhofer region (far-field) and actual distance depends on the size of the source and wavelength.

Figure 19. Far-field criteria. Source: [20].

In the case of the source we employed, R_0 is $R_0 = 0.1016\ m$, the frequency sweep was done from 50 Hz to 400 Hz, and the corresponding λs in water are

$$\lambda(60Hz) = \frac{1500\frac{m}{s}}{50\ s^{-1}} = 30\ m\ , \qquad (3.9)$$

$$\lambda(400Hz) = \frac{1500\frac{m}{s}}{400\ s^{-1}} = 3.75\ m. \qquad (3.10)$$

Therefore, the range to the far field of the source with R_0 = 0.1016 m is

$$r(60Hz) = \frac{\pi \cdot (0.1016\ m)^2}{25\ m} = 0.0013\ m, \qquad (3.11)$$

$$r(400Hz) = \frac{\pi \cdot (0.1016\ m)^2}{3.75\ m} = 0.0086\ m. \qquad (3.12)$$

The measurement was made at a frequency of 120 Hz while rotating the sensor around its axis and 1,167 samples were taken. The data acquisition was made with NPS's portable data acquisition system, in addition to installed equipment at TRANSDEC. The distance between the source and the sensor was about 2 m.

Figure 20 shows measured directional dependence of the signal when the sensor is rotated by 360 degrees. The data was plotted using linear scale in (a) and polar plot in (b). It clearly shows the expected cosine dependence typically associated with velocity or pressure gradient sensors. The cosine dependence response can be used to obtain baring of sound sources. The symmetry of the response about the axis normal to the sensor generates an ambiguity, however, and in Chapter V an approach for resolving this will be discussed.

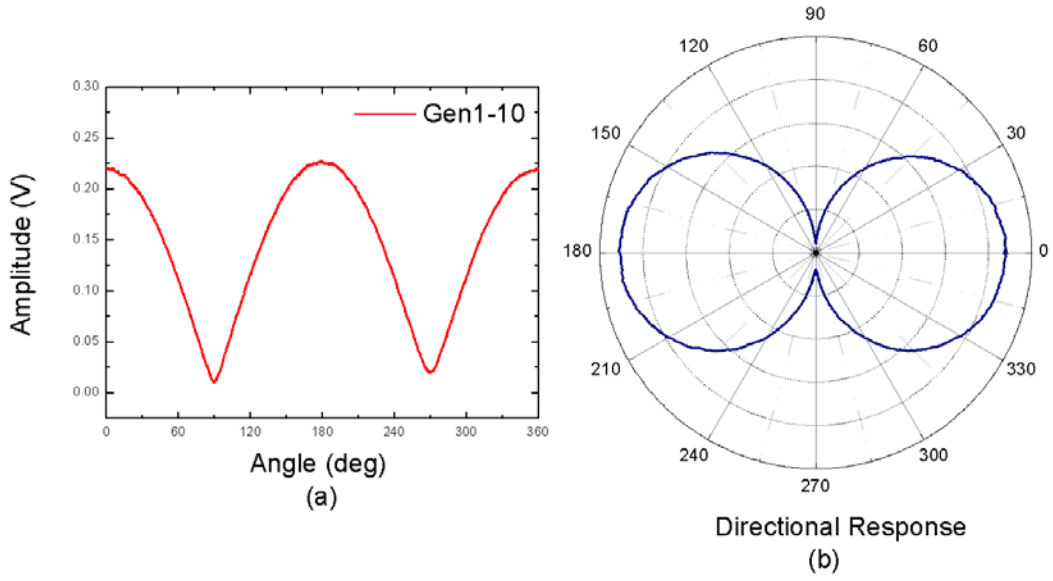

Directional response of the sensor (a) in Cartesian coordinates and (b) using polar coordinates.

Figure 20. Directional response of the Gen1-10 sensor.

THIS PAGE INTENTIONALLY LEFT BLANK

IV. EFFECTS OF SENSOR HOUSING

A. PROBLEM DESCRIPTION

Measurements of the Gen1-10 sensor frequency response showed additional features when compared with the simulated frequency response, as shown in Figure 21. The frequency response is obtained by dividing the sensor response by a reference hydrophone, which is normally flat over the frequency range of interest (see Appendix A).

In Figure 21, it is possible to observe three different regions where the sensor shows frequency response different than the simulated one. One of the frequencies, in the low frequency range, is related with the frequency of resonance of the source, which disturbs the response of the sensor, producing a result different than the expected. The other peaks (highlighted in Figure 21) might be due to the sensor housing (boot).

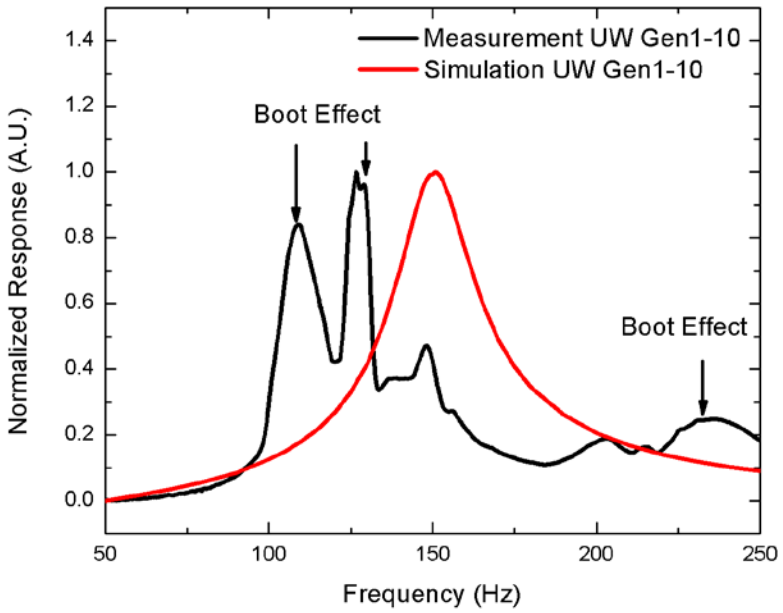

Measured frequency response (black line) of a Gen1-10 MEMS sensor using NPS water tank after the division of the reference hydrophone. Also included is simulated response (read line) using COMSOL.

Figure 21. Comparison of measured and simulated responses.

In order to investigate this issue, two tasks were conducted. In the first, the reference hydrophone (B&K 8103) was enclosed using the same housing used for the sensor to eliminate the boot effect from the measurements. In the second, COMSOL simulation was carried out by introducing a spherical boot to emulate the experimental arrangement.

B. ENCLOSED HYDROPHONE EXPERIMENT

1. Measurements

The motivation of this experiment was to test the enclosure effect using a hydrophone with known characteristics and verify whether the enclosure affects its frequency response. Two B&K 8103 hydrophone were selected due to their flat response over the frequency of interest and small dimensions. One hydrophone was placed inside an enclosure similar to that used for the MEMS sensors. During the measurement, the two hydrophones were placed close to each other as shown in Figure 22 to compare their responses. The UW speaker UW30 was used as a source (see Appendix C). Source and receivers were tested at the NPS water tank according to a block diagram, as shown in Figure 23.

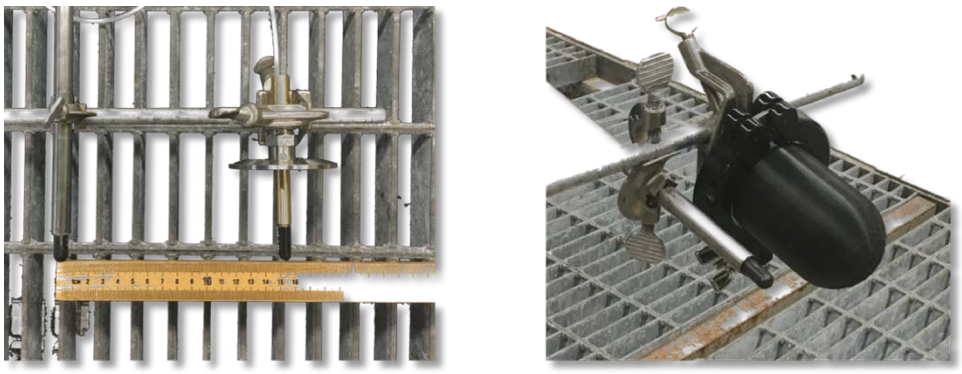

The picture shows the two hydrophones mounted in close proximity to compare their responses. Their output signals were recorded simultaneously.

Figure 22. B&K 8103 hydrophones with and without enclosure.

The test was carried out at NPS's water tank in the low frequency range (50–400 Hz). The experimental setup is the same as that used by TRANSDEC and schematically shown in Figure 15.

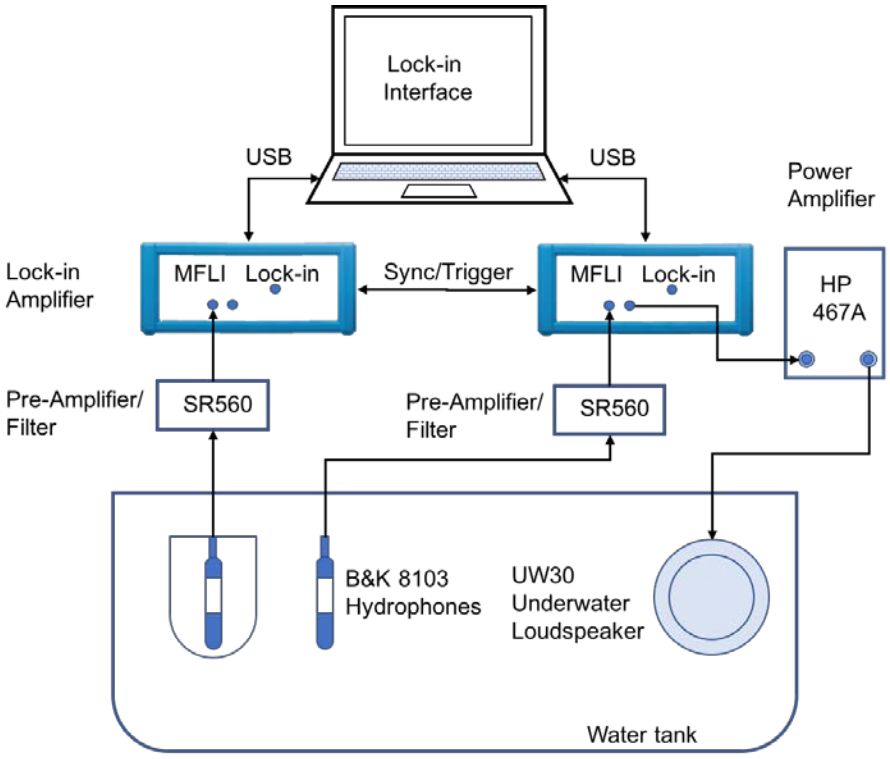

Figure 23. Schematics of the measurement setup.

2. Results

Figure 24 shows measured sound intensities from UW30 source using two hydrophones with and without the housing (boot). The test shows that the enclosure attenuates the source resonance and adds an extra enhancement at around 250 Hz. More interesting is that the effects of the enclosure beyond 500 Hz are almost negligible. This suggest that the enclosure, due to the type material (urethane Flexane 80) and its volume, interferes with the operating frequency range of the sensor. The material selected for the enclosure is urethane; this type of material may contain air, which can produce bubbles during the curation process. These bubbles can affect the acoustic characteristics of the boot.

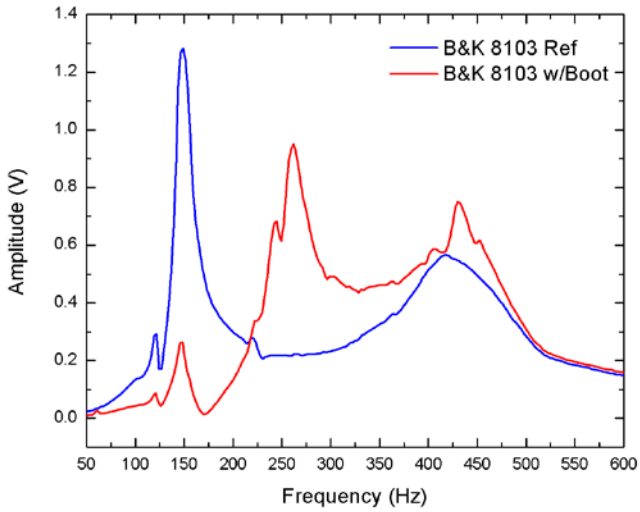

Comparison between the reference hydrophone with and without enclosure. The presence of the boot reduces the response in the low frequency range (50–200Hz) while gaining between 225–400 Hz. This effect is minimal above 400Hz.

Figure 24. Reference hydrophone frequency response with and without boot.

Figure 25 shows the ratio of hydrophone responses in Figure 24. The discrepancies are evident when the curve deviates from the unity.

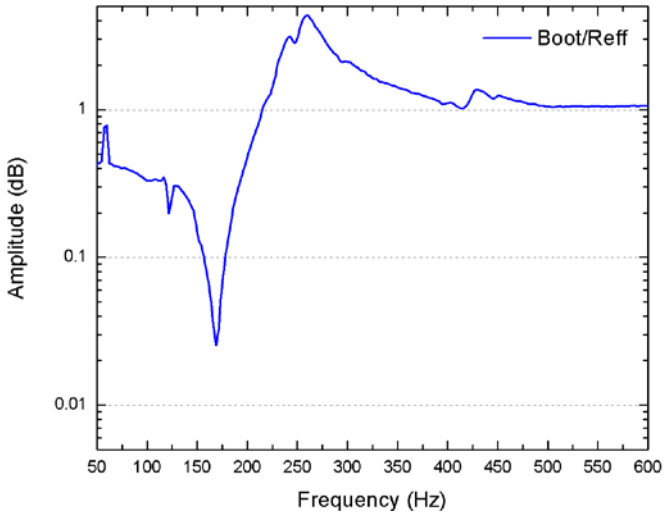

The figure shows the relationship between the hydrophone with the boot and the reference hydrophone. The y-axis is set in log scale to show details of the boot effect. It can be seen that the presence of the boot does not affect frequencies beyond 400 Hz.

Figure 25. Ratio of responses with and without boot.

The complex enclosure configuration and non-uniform distribution of bubbles within the boot material make it difficult to analyze their effects on the sensor analytically. One approach is to model the presence of the enclosure using FEM simulation assuming an isotropic spherical shell surrounding the sensor.

C. COMSOL SIMULATION OF BOOT EFFECT

To understand of the effect of the boot on the sensor performance, a COMSOL model was built by surrounding the sensor with a spherical shell with approximately the same volume as the actual enclosure used in the measurements. For this model, a Gen1-10 sensor without combs and TA physics was used. The parameters of the sphere were radius of $r_{eq} = 31.5\ mm$, according to (4.2), and a thickness of 3 mm

$$V_{boot} = V_{cylinder} + V_{hemisphere} = h \cdot \pi \cdot r^2 + \frac{2}{3} \cdot \pi \cdot r^3 \qquad (4.1)$$

$$V_{eq} = \frac{4}{3} \cdot \pi \cdot r_{eq}^3 \therefore r_{eq} = \sqrt[3]{\frac{3}{4} \cdot h \cdot r^2 + \frac{r^3}{2}}, \qquad (4.2)$$

where *h = 50 mm* and *r = 25 mm*.

The Young's modulus of the urethane Flexane 80 was obtained using an Instron model 1000 stress measurement system. The stress was on the sample calculated using the measured force under tension divided by the initial area of the tested region of the sample. The sample was held in place using two pneumatic clamps, one on each end. Both the stress and the displacement were collected simultaneously as a function of time to extract stress and strain. The strain rate was 5"/minute. The value obtained for the Young's modulus was 0.23 MPa; this value is critical to model an accurate response. In this model, no microbubbles were considered for simplicity.

1. Model Description

In order to incorporate the boot into the model, a separate SM physics has to be introduced to describe it. The complete model is a series of Multiphysics interactions. First, the PA physics interact with the TA physics layer surrounding the boot, then the TA

physics interact with the SM physics to take into account the boot, and finally a second TA layer interacts with the sensor as illustrated in Figure 26. In Figure 26, the darker sphere represents the enclosure. The small sphere close to the sensor was designed to facilitate the meshing.

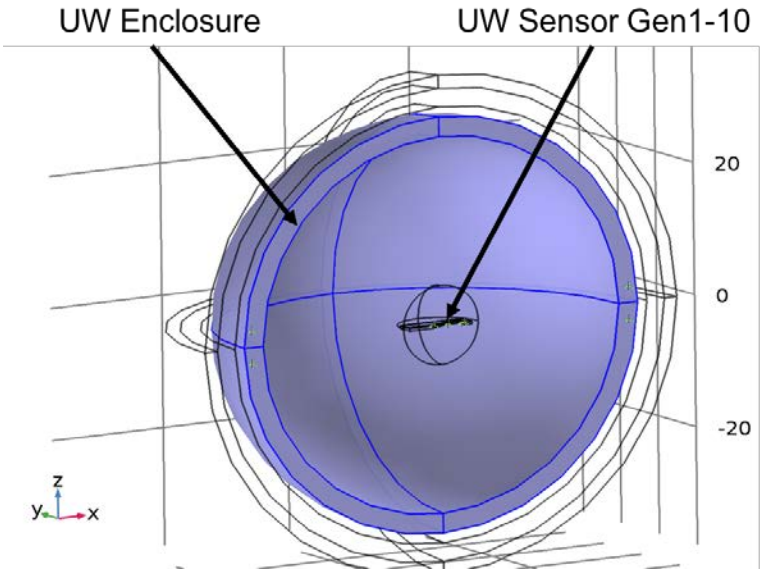

COMSOL model showing the geometry used to emulate the boot effect.

Figure 26. COMSOL model including the boot and Gen1-10 sensor.

2. Simulation Results

Two types of studies were performed. The first study was to determine the effects on the frequency response of the sensor. The second study varied volume and Young's modulus in a parametric sweep to find out ways to minimize the boot effect.

Figure 27 shows the frequency response of the Gen1-10 without the enclosure. The frequency response shows only the resonance frequency of the sensor over the simulated frequency range from 60 Hz to 1000 Hz.

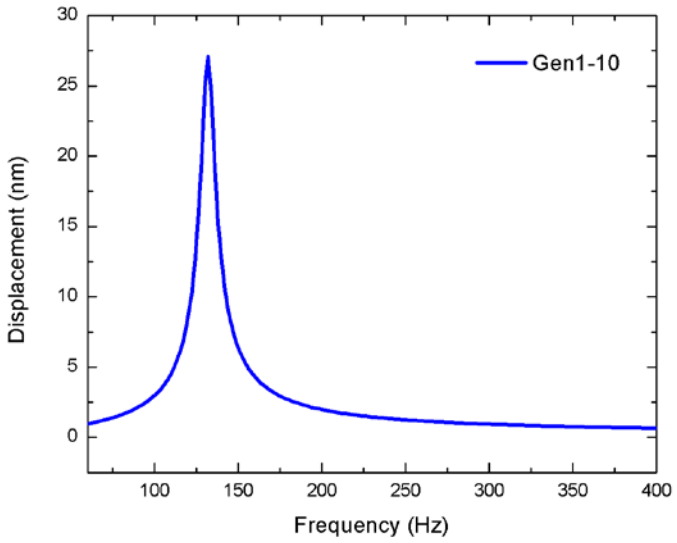

Simulated Gen1-10 sensor frequency response without the enclosure surrounded by water.

Figure 27. Simulation of the sensor without the enclosure.

Figure 28 shows the displacement amplitudes of the sensor (black) and enclosure (red) when the boot is included on the simulation. A logarithmic scale was used in the y-axis to show greater details of the effect of the enclosure. The simulation with the enclosure shows a similar behavior to that of the measurement in Figure 24, despite the simple geometry of the boot. The resonant feature of response of the enclosure in the simulation is overestimated due to lack of damping associated with the boot in the simulation. The simulation shows that the frequency response of the enclosure affects the response of the sensor, increasing its sensitivity where the boot has a resonance.

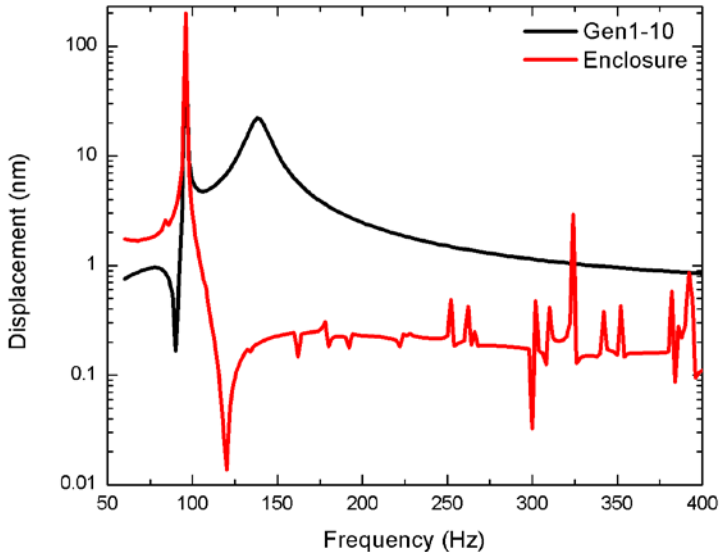

Simulated vibration amplitudes of sensor (black) and a point on the surface of the boot (red). The displacement of the boot shows that it interacts with the sensor response.

Figure 28. Frequency responses of the sensor and a point on enclosure.

A third simulation was made with a smaller boot volume (half of the radius) and parametric sweep of Young's modulus. The Young's modulus of the enclosure was taken to be 0.23 MPa, 1 MPa, and 100 MPa in the simulation. The results show that reducing the volume of the enclosure shifts the unwanted resonance frequency of the boot. In addition, resonant frequency of the boot is found to increase with the Young's modulus. Therefore, a smaller enclosure with a higher Young's modulus would move the frequency response of the boot away from that of the sensor, reducing the interference, as shown in Figure 29.

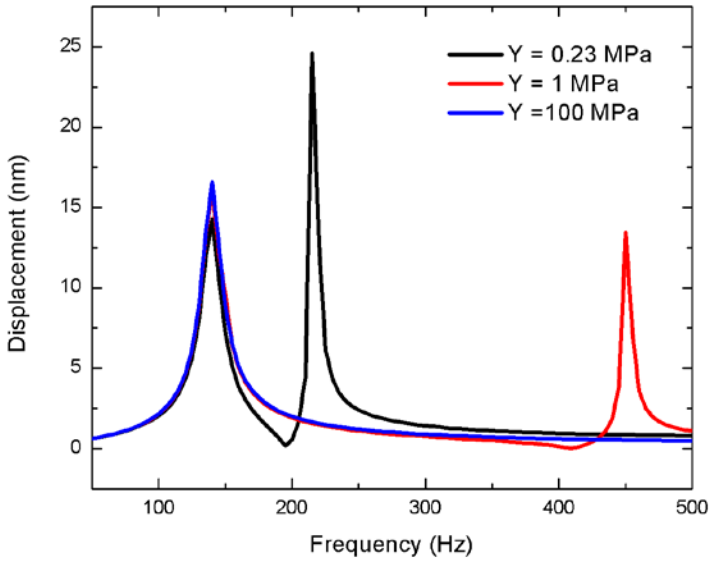

Simulated frequency response of amplitude of vibration of Gen1-10 sensor in water using a smaller boot volume (radius of 15.5 mm) for a set of Young's moduli.

Figure 29. Frequency response of sensor with different boot parameters.

Figure 30 shows the vibration amplitude of a point on the boot for the same set of Young's moduli. It correlates well with that of the sensor responses in Figure 29.

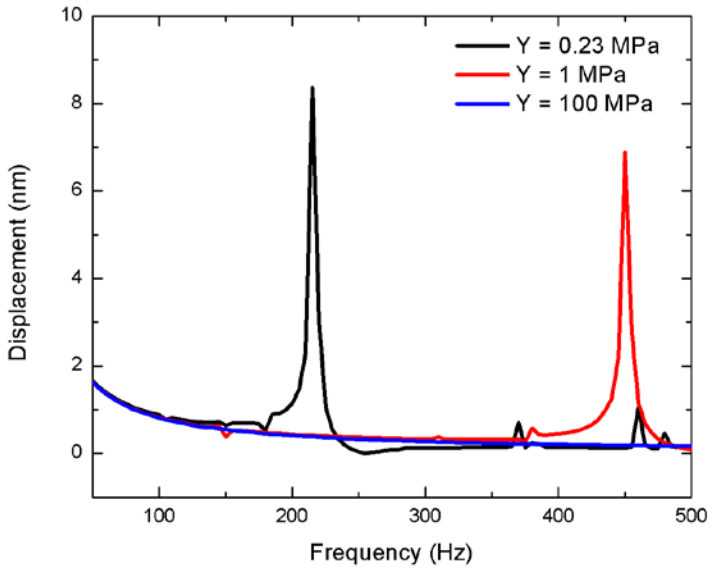

Simulated frequency response of amplitude of vibration at a point on the enclosure with a smaller boot volume (radius of 15.5 mm) for a set of Young's moduli.

Figure 30. Enclosure frequency response.

THIS PAGE INTENTIONALLY LEFT BLANK

V. CANTED SENSORS FOR DETERMINING DIRECTION

A. BACKGROUND

As described earlier, when the bending mode is employed for detection there is ambiguity in determining the angle of arrival due to symmetry of the response about an axis normal to the sensor (see Figure 4). To overcome this ambiguity, a canted angle configuration can be used. According to [21], two sensors can be placed to create a sensor assembly and solve the angle ambiguity, illustrated in Figure 31.

In the assembly, both sensors are symmetrically placed with an offset angle. Since each sensor produces an output proportional to the net pressure (P) at the sensor, giving a cosine dependence $P = |aP_0 \cos(\theta)|$, the azimuthal angle ambiguity in the xz-plane can be solved [21]. In order to get the same sound pressure amplitude in both sensors, they are placed in close proximity to each other compared to the wavelength of incident sound.

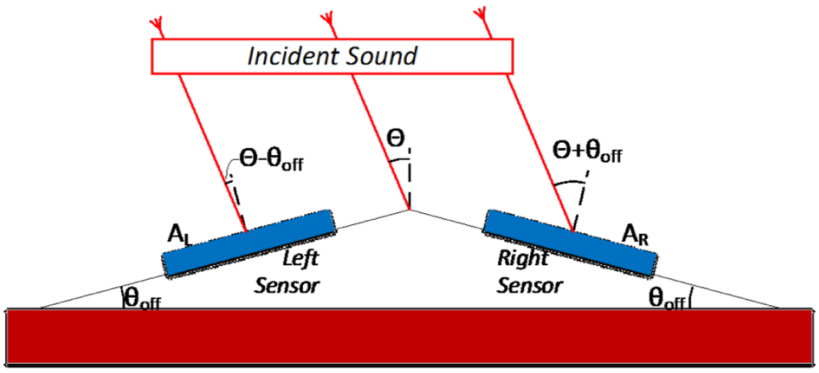

Schematics of two-sensor assembly; the sensors are co-located at an angle θ_off such that the incident sound will interact at $\theta - \theta_{off}$ at the left sensor and $\theta + \theta_{off}$ at the right sensor.

Figure 31. Two-sensor arrangement to solve angle ambiguity. Source: [21].

According to [21], the ratio of difference over sum of the two responses to an incident plane wave can be derived, and has the form given in Equation (5.1)

$$\frac{P_L - P_R}{P_L + P_R} = tan(\theta_{off})\, tan(\theta), \qquad (5.1)$$

where P_L is the pressure in the left sensor P_R is the pressure in the right sensor, θ_{off} is the offset angle of the mounting, and θ is the incidence angle of sound wave as shown in Figure 31.

The expected angle response of the sensor is twice the offset angle, as shown in Figure 32.

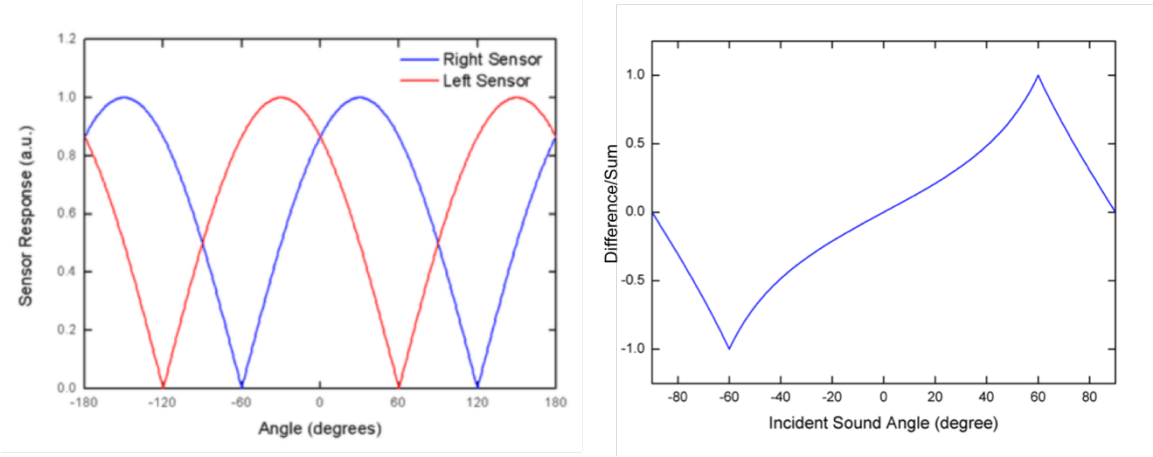

Expected response of 30º-offset canted angle configuration. The figure on the left shows the simulated sensor response. The angle difference of the sensors is 60º. The figure on the right shows the difference over the sum of the simulated sensor response.

Figure 32. Simulated responses for 30º canted angle. Adapted from [21].

B. EXPERIMENTAL SETUP

In order to fully understand the effects of the offset angle, and the size of the assembly, three different configurations by varying the canted angle were tested. For this test, two MEMS sensors from the same batch were selected and mounted symmetrically, as schematically shown in Figure 31. Frequency responses of the sensors were done in the lab using a Polytec OFV-5000 laser vibrometer and anechoic chamber using electronic readout. Measured frequency responses using the laser vibrometer and electronic readout are shown in Figures 33 and 34, respectively. The two sensors were found to have nearly identical frequency characteristics.

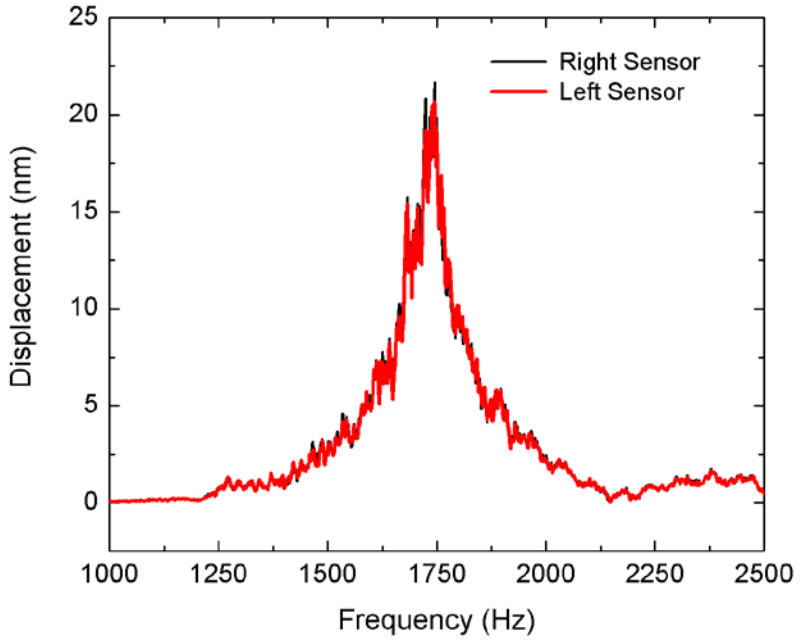

Displacement amplitude as a function of frequency for the two sensors measured using a laser vibrometer when θ = 0 degree (or normal incidence).

Figure 33. Frequency response of displacement amplitude.

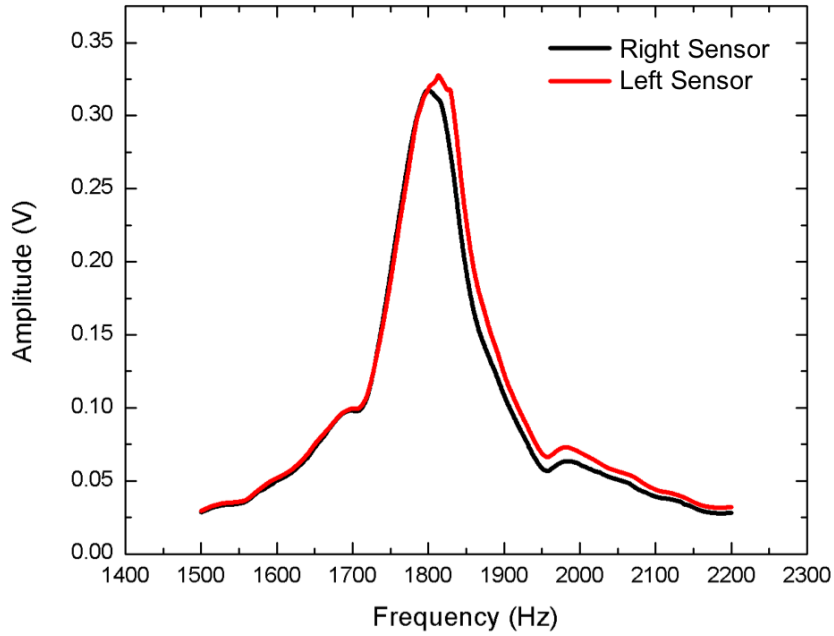

Measured frequency response of electronic output of two sensors in the anechoic chamber at normal incidence.

Figure 34. Frequency responses of electronic output of two sensors.

Three different offset angles, 30º, 45º, and 60º, were used to test the DF sensor in air, as shown in Figure 35.

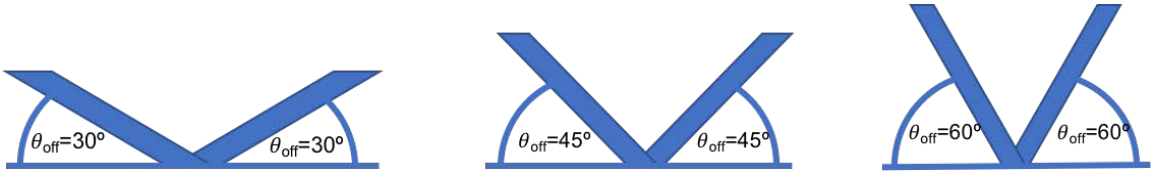

Figure 35. Canted angles configurations (30º, 45º, and 60º) employed in the measurement.

The sound source was a JBL 2380A Bi-radial horn. Two MFLI Zurich lock-in amplifiers were used for data acquisition. The speaker was connected to reference output of the master lock-in amplifier via a power amplifier, as shown schematically in Figure 36. The sensor assembly was mounted to a B&K Type 5997 turntable controller that was attached to the ceiling of the anechoic chamber. One of the lock-in amplifiers supplied 5 VDC to the sensors and the sensor outputs were connected to the lock-in amplifiers. The output waveforms from the sensors were measured using a computer interfaced to the lock-in amplifiers. In order to acquire the data simultaneously, both lock-in amplifiers must be synchronized with a master-slave configuration (see Figure 36). To accomplish this, a LabOne Web Server application is launched in the host computer. This allows control of both lock-in amplifiers as well as their synchronization. The data was extracted in a CSV file for post processing [22]. For testing the angular responses of the two sensors, the sound frequency was set at 1745 Hz. The sound level was adjusted using the power amplifier until a good SNR was observed without saturating the lock-in amplifiers. The turntable was set up for 1-minute rotations.

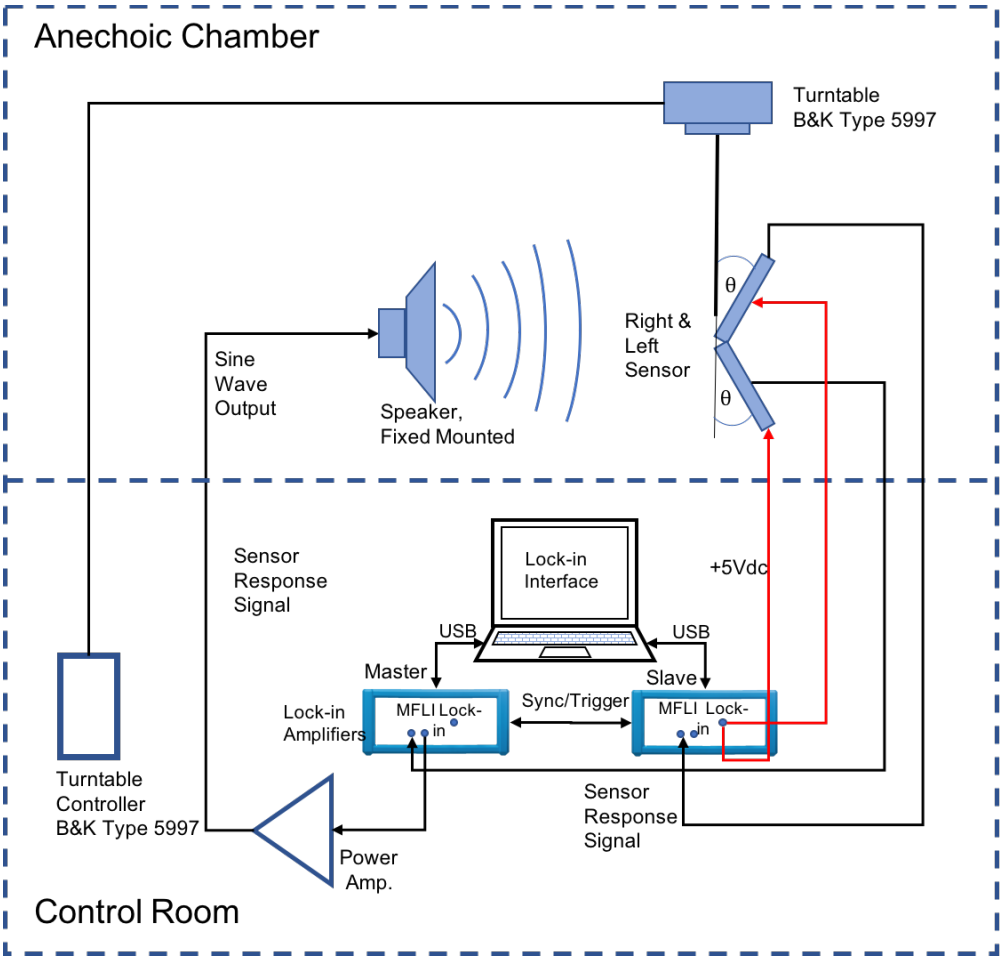

Figure 36. Block diagram of the test setup used for extracting electronic signals in the anechoic chamber measurement.

C. DATA ANALYSIS

Figure 37 shows measured directional responses of the two sensors for 30º canted angle configuration. The measurements show an angle difference of 18.4º, which is much less than the 60º expected based on the geometry of the assembly (see Figure 32). Nevertheless, with this configuration the system is capable of covering more than the expected 120º. The effective canted angle θ_{eff} of 9.2º (half of the offset angle) reduces the magnitude of the difference over the sum (see Figure 37) based on Equation 5.1. The measured difference over sum data was fitted using the θ_{eff} and found to be in close agreement. It is suspected that the printed circuit boards (PCBs) could alter the directional

response. Therefore, a simulation with COMSOL was conducted to understand the observation.

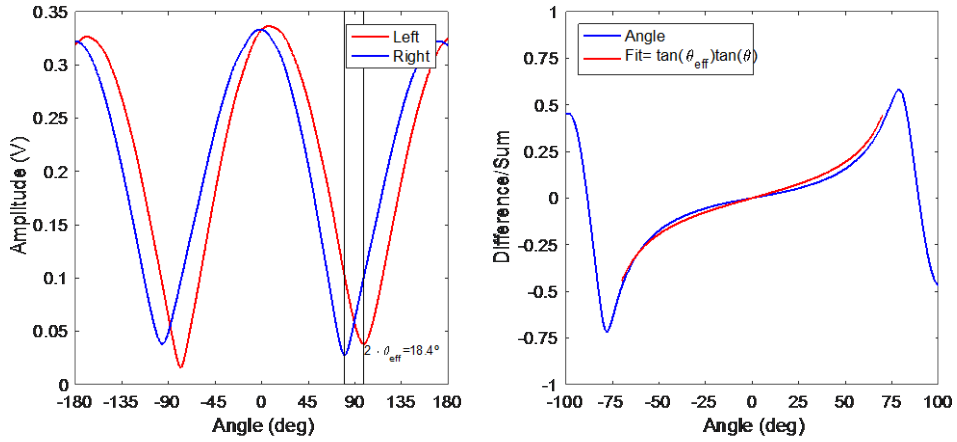

The simultaneous measurement of directional responses of the two sensors are shown on the left with an effective canted angle of 9.2º. The difference between two minima defines the effective offset angle. The figure on the right shows the difference over the sum of the two sensor responses (blue). Fit of the data using the effective canted angle shows good agreement with the measurements.

Figure 37. Measured responses for 30º canted angle.

For the 45º angle, the measurements show an angle difference of 34.9º, as shown in Figure 38. The fit based on θ_{eff} of 17.45º starts to deviate as the incident angle increases (see Figure 38). This may be due to the influence of the one sensor's circuit board on the other sensor's response.

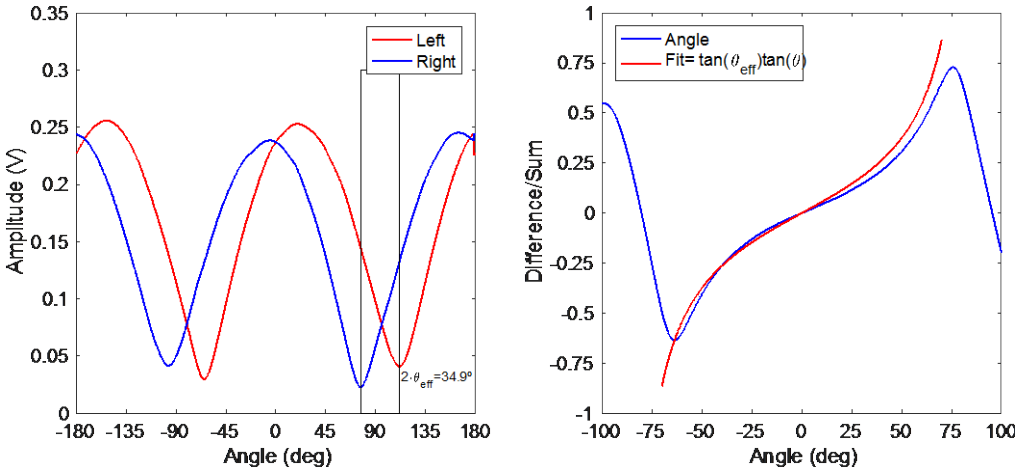

Directional responses of the two-sensor assembly, which showed an angle difference of 34.9º. The graph on the right shows the difference over the sum for the data shown on the left graph. The fit using an effective canted angle of 17.5º gives good agreement for low-incidence angles and somewhat deviates at higher angles.

Figure 38. Measured responses for 45º canted angle.

For the 60º angle, the measurements show angle difference of 43.6º, as shown in Figure 39. At this angle the measured directional characteristics deviate from the expected cosine behavior. The fit based on θ_{eff} of 21.8º shows a reasonably good agreement with difference over sum data from the measurement (see Figure 39).

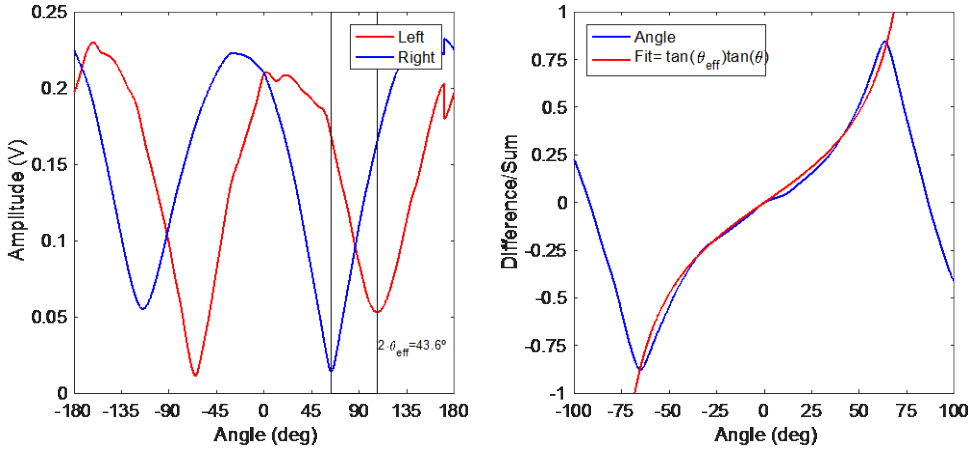

The figure on the right shows the simultaneously response of the sensors with an effective offset angle of 21.8º. The figure on the left shows the difference over the sum of the left and right sensors, (Left - Right)/(Left + Right). The two fit curves are overlapping to show the accuracy of the fit.

Figure 39. Measured responses for 60º canted angle.

D. ACCURACY OF MEASURED ANGLE

For determining the uncertainty of measured angles, 121 data points were taken between -60º and 60º degrees from the difference over the sum data for all three canted angles. The data was fitted to Equation (5.2) to obtain a fitting parameter (α) that best represents the measurements. In addition, the incident angle was obtained using the measured canted angle, θ_{eff} using equation (5.3). Fitting was done using cftool of MATLAB.

$$\theta = atan\left(\frac{\left(\frac{P_L - P_R}{P_L + P_R}\right)}{\alpha \cdot tan(\theta_{off})}\right) \tag{5.2}$$

$$\theta = atan\left(\frac{\left(\frac{P_L - P_R}{P_L + P_R}\right)}{tan\left(\frac{\theta_{eff}}{2}\right)}\right) \tag{5.3}$$

Figures 40 and 41 show plots of fitted curves for 30º canted angle using Equations 5.2 and 5.3 as well as difference between measured and estimated angles. The results show that both methods can be used to give a reasonable R-square. Comparing the first two methods, the best result was achieved with the 30º canted angle with a correction factor, which improves the fit by 2%. Looking closely at the residuals, for a 30º canted angle, the second method shows an error of less than 3º over a wide range of angles as shown in Figures 40 and 41. An optimal result can be achieved with a look-up table, which is the exact response of the system.

The R-square for the 30º canted angle using Equation 5.2 was found to be 0.9961 and the corresponding residuals were found to be between 2 or 3 degrees at 20º incident angle, as seen in Figure 40. Using θ_{eff}, the estimated residual was greater and reaching up to 7º for the same angle of incidence, however, as seen in Figure 41.

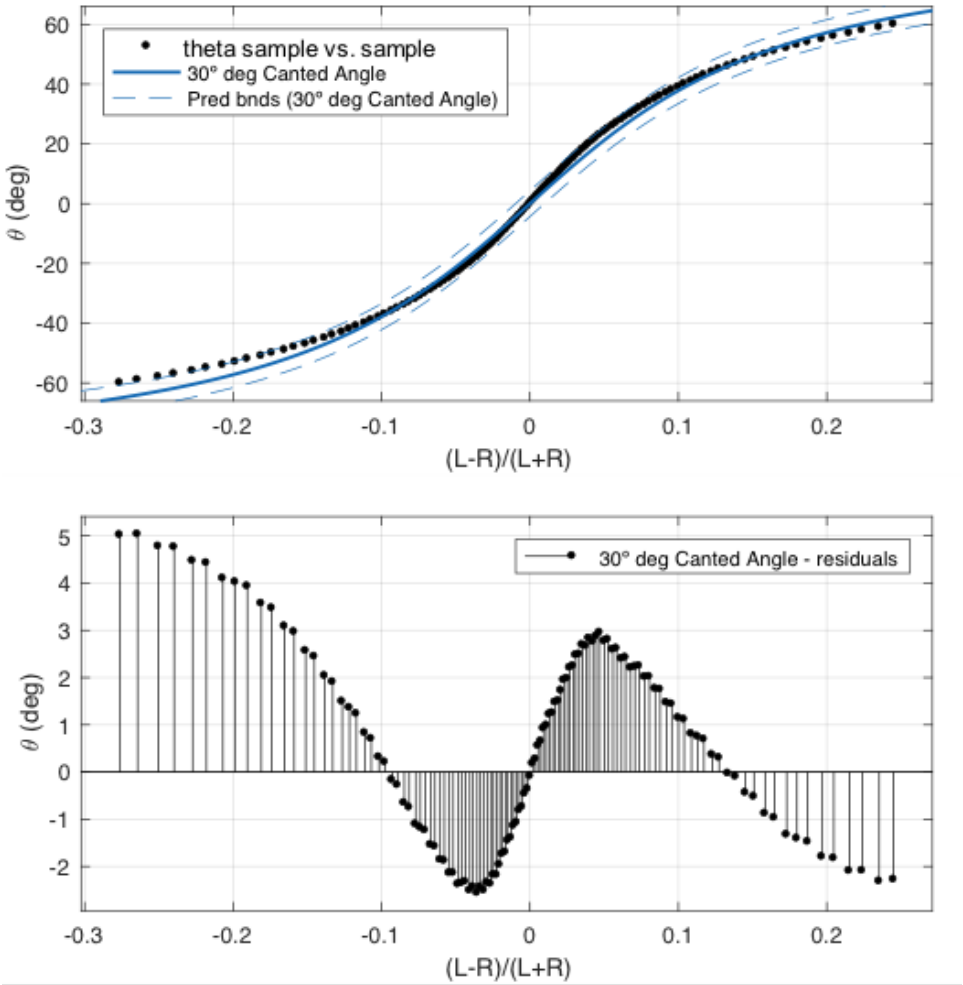

The top plot shows fitting of data to determine the factor α. The dashed lines show the 95% confidence interval for the fit. The bottom plot shows the residuals compared to the actual. The error of angle is within 3º for most of the range of interest.

Figure 40. Fitting curve to find α and residuals for canted angle of 30º.

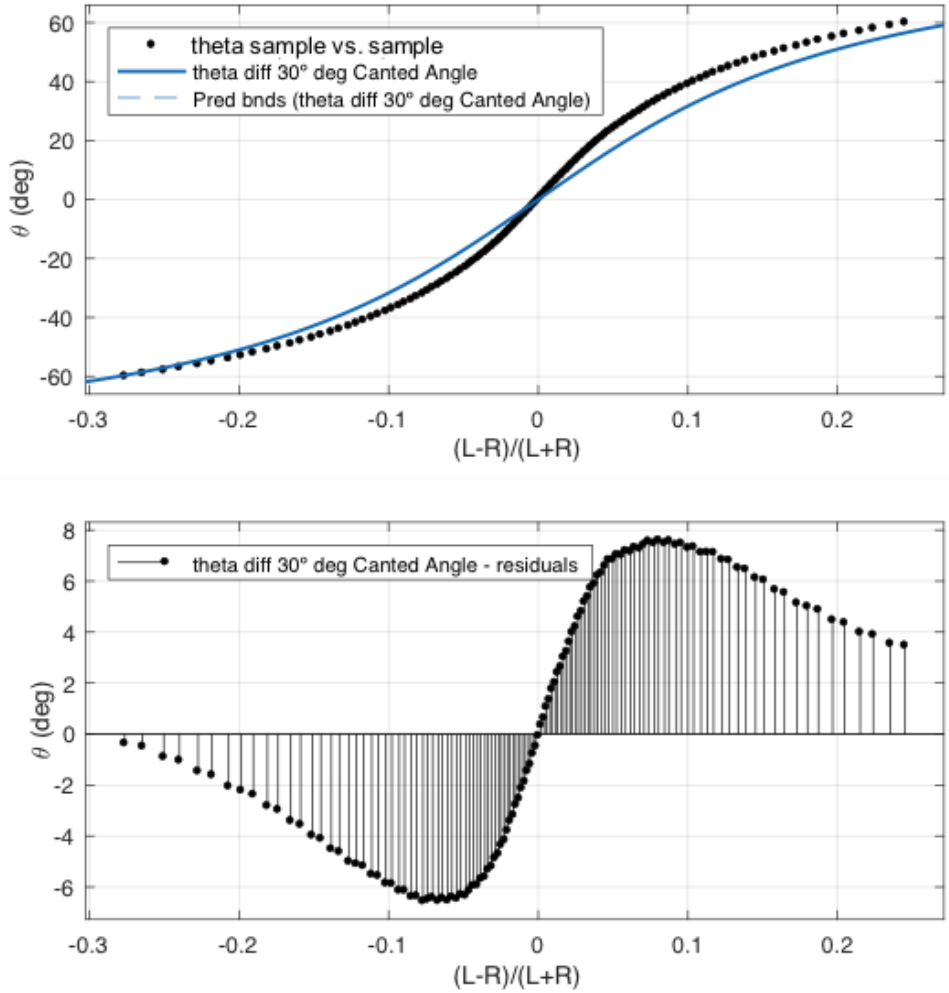

The top plot shows fitting of data using the effective canted angle. The fit exceeds the 95% confidence interval. The bottom plot shows the residuals compared to the actual. The error of angle is within 8º for most of the range of interest.

Figure 41. Fitting curve using θ_{eff} to find residuals for canted angle of 30º.

Table 1 summarizes the fitting parameters extracted and their confidence levels.

Table 1. Fitting parameters and error analysis for canted angles.

Model	$\theta = \text{atan}\left(\frac{\left(\frac{P_L - P_R}{P_L + P_R}\right)}{\alpha \cdot \tan(\theta_{\text{off}})}\right)$			$\theta = \text{atan}\left(\frac{\left(\frac{P_L - P_R}{P_L + P_R}\right)}{\tan\left(\frac{\theta_{\text{eff-off}}}{2}\right)}\right)$	
Canted Angle	Coefficient w/95% CI	R-square	Adjusted R-squared	R-square	Adjusted R-squared
$\theta_{off} = 30º$ $\theta_{eff-off} = 18.4º$	**α = 0.223** (0.2189, 0.2271)	0.9961	0.9961	0.9746	0.9748
$\theta_{off} = 45º$ $\theta_{eff-off} = 34.9º$	**α = 0.2812** (0.2751, 0.2874)	0.9944	0.9944	0.9898	0.9899
$\theta_{off} = 60º$ $\theta_{eff-off} = 43.6º$	**α = 0.2368** (0.2318, 0.2419)	0.9948	0.9948	0.9946	0.9946

The table shows the two models to fit the tangent for the different canted angles. For the (α) factor the model have a 95% CI for the fitting curve. The model with half of the offset angle shows that their values are away from the 95% CI. The R-square represents the error of the fitting for each model while the Adjusted R-squared takes into account the number of samples to measure the fitting.

E. COMSOL SIMULATION OF CANTED ANGLE ASSEMBLY

It was observed, using the measured simultaneous directional responses of the canted sensor assembly, that the offset angle calculated disagrees with the actual offset imposed by the assembly. It is suspected that interaction of sound with the PCBs used for mounting the sensors could alter the directional responses. In order to understand the observations, a COMSOL simulation was carried out with the PCBs. Figure 42 shows the simulated responses of the canted sensors, with and without PCBs of the actual dimension (see the inset).

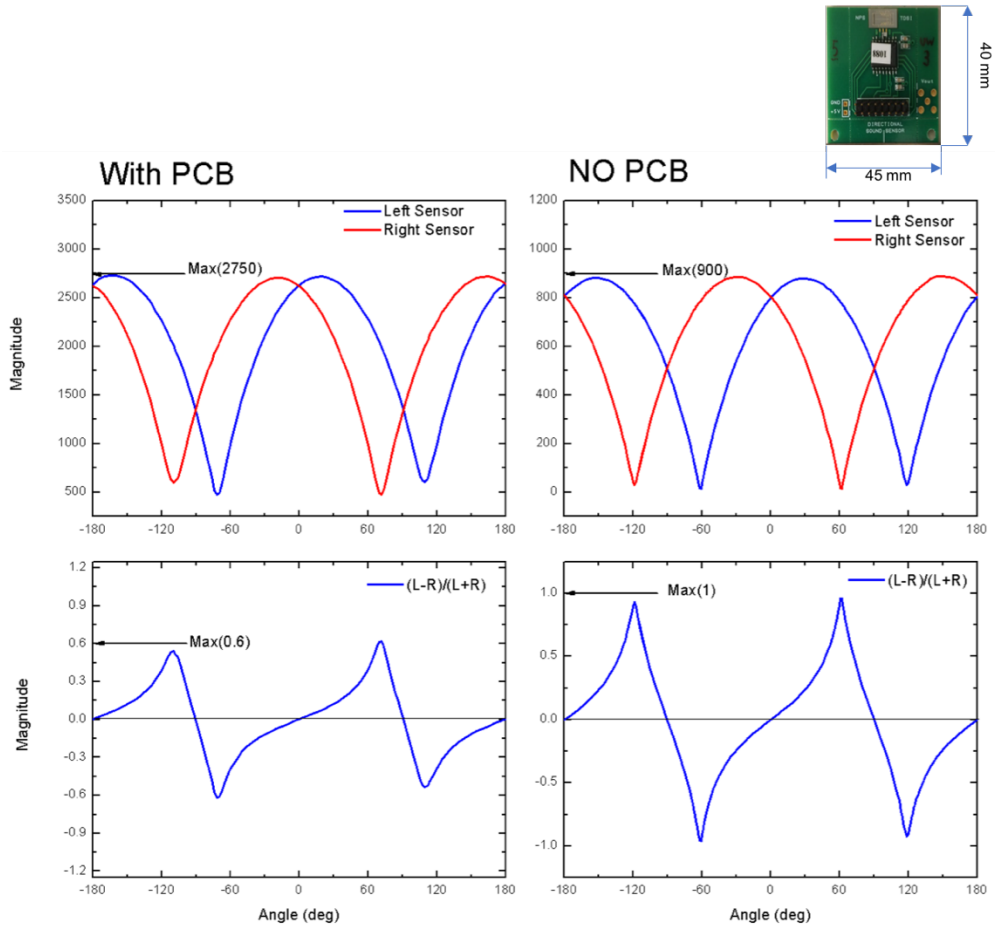

The graphs on the left column shows the results of a COMSOL simulation with the actual size of the PCB, while the graphs on the right column shows the simulation with a much smaller PCB size. The slope of the relation (L-R)/(L+R) decreases when the PCB is added.

Figure 42. Canted angle COMSOL simulation.

Simulations show that indeed the PCB affects the combined directional response, therefore requiring correction to Equation (5.1) to obtain the angle of arrival (θ). It was found that the scattered sound field was altered when the PCBs were included in the simulation.

Three methods can be used to improve the accuracy of the directional of arrival. The first method is to use a look-up table using the actual data. The second method is to use a correction factor (α) for Equation (5.1). The third method is to use an effective canted angle, which is half of the measured offset angle in Equation (5.1).

VI. CONCLUSION

A. SUMMARY

Acoustic sensors operating in UW environments were designed and fabricated based on the *Ormia ochracea* fly's hearing organ. The design of the sensors was carried out using COMSOL Multiphysics software to accurately determine the sensor characteristics. The modeling included interaction of sound with the MEMS structure via the thermoviscous module, which takes into account the mass loading and viscous damping. The optimized sensors were fabricated using MEMSCAP commercial foundry service. The testing of the sensors was performed using NPS water tanks as well as TRANSDEC UW testing facility in San Diego.

For the UW characterization of the sensors, a custom housing was made to immerse the sensors in a non-conducting fluid with acoustic impedance close to that of water. A low-viscosity silicone oil was selected as the fluid for immersing the sensors due to its desirable electrical and fluid characteristics. Measurements showed that the sensors were able to detect UW sound with a narrow-band spectral response. The measured spectral response is in good agreement with that of the simulations, validating the accuracy of the modeling. In addition, directional response of the sensors was also measured and found to have the expected cosine dependence, indicating their ability to detect the bearing of UW sound sources.

During the measurement, it was found that the boot used for enclosing the sensor affected the measurements due to its non-uniform response to the incident sound. Initially, a reference hydrophone was enclosed in a similar enclosure to reduce the boot effect. Detailed COMSOL simulations were carried out to understand this effect. The results show that the enclosure produced unwanted resonance frequencies, in the frequency range of interest primarily due to its dimensions. The resonances of the enclosure were found to excite the sensor, giving a false frequency response.

For uniquely determining the bearing of sound sources, it is necessary to use two sensors at a canted angle to eliminate symmetrical (cosine) response of individual sensors.

A detailed study was carried out to understand the effect of the canted sensor assembly on the directional responses. It was found during the measurements that circuit boards used in integrating the sensors affected directional responses, which needed to be included for accurate determination of the direction. To understand this effect, COMSOL simulations were performed including the actual size of the circuit boards. Simulations were found to agree well with the experimental observations when the circuit boards were included. Several approaches to determine the angle based on these observations were presented in the thesis.

The research carried out during the course of this thesis provides important information on the design, fabrication, and packaging of MEMS-based sensors for UW applications.

B. RECOMMENDATIONS FOR FUTURE WORK

The boot effect has a great impact on the overall response of the sensor. A refinement of the boot fabrication process as well as its dimensions need to be further explored to eliminate its effects on the sensor response. For example, increasing the Young's modulus of the enclosure or reducing the volume could move the unwanted resonance of the boot away from the frequency response of the sensor.

Currently, the direction is uniquely determined using two sensors mounted at a canted angle. Placing two sensors in the same enclosure implies a new hardware design, however, including additional cabling as well as the readout electronics. Using a two-wing MEMS sensor and reading signals from both wings separately, it may be possible to do the DF using only one sensor. This is possible due to the coupling of the rocking and bending modes, giving two different vibration amplitudes at the wings.

APPENDIX A. HYDROPHONE TYPE 8103

SENSITIVITY

$$M_L(dB) = -211.5 \text{ dB re } 1V/\mu Pa$$

DIMENSIONS

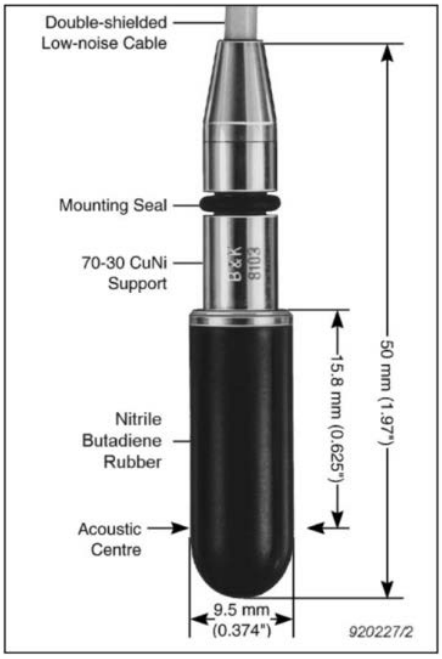

FREQUENCY RESPONSE

dB re 1V/µPa

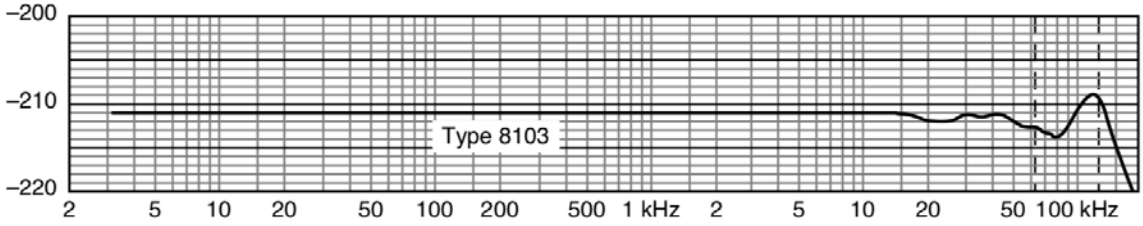

DIRECTIVITY PATTERN

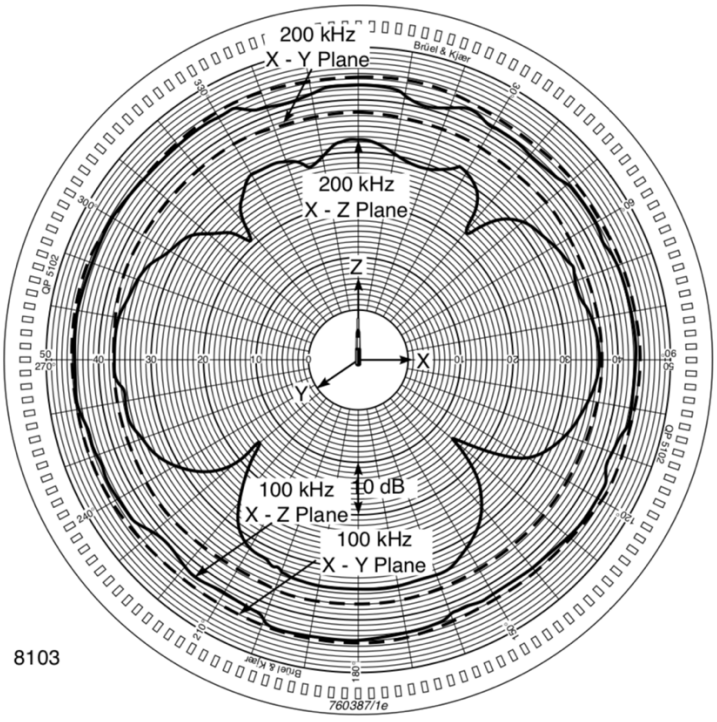

8103

APPENDIX B. LUBELL VC2C UNDERWATER ACOUSTIC TRANSDUCER

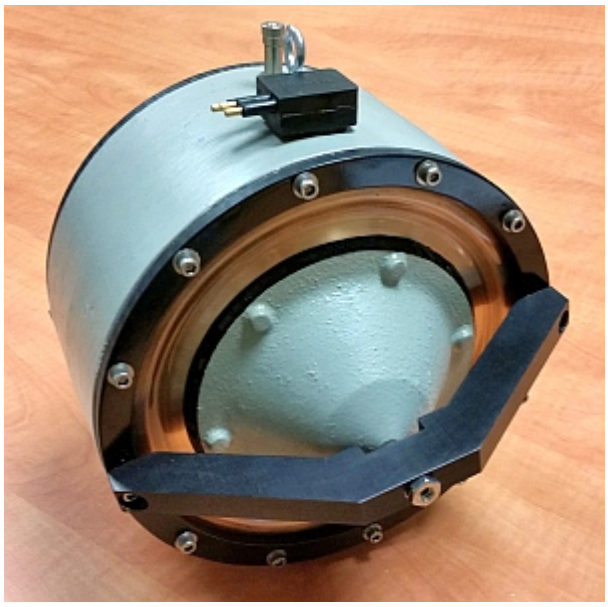

SPECIFICATIONS

Description:	Axial symmetric double piston radiator with spring copper diaphragms and external stops
Frequency Range:	50 Hz to 1.5 kHz
Resonant Frequency:	115 Hz +/- 5 Hz
Impedance:	Varies with frequency (4 ohms minimum @ 50 Hz; 17 ohms @ 1500 Hz)
Maximum Output Level:	174dB/uPa/m
Maximum Voltage/Current:	20 Vrms/2.5A (100% duty-cycle)
Q Parameters:	Qtco~2.5 Qmc~5
Directivity:	Omnidirectional to 1.5 kHz
Cable:	Teledyne Marine LPIL-3-FS on 50 feet of 16/3 SO
Operating Depth:	10 feet (3.05 meters) minimum, 50 feet (15.24 meters) maximum
Maximum Air Pressure:	23 psi (WARNING: use provided hand air pump only!)
Piston Stop Gap:	0.016 inches (Schrader valve pin depressed to equalize internal/external pressure)
Dimensions:	8”D x 9.75”L
Weight:	21 lbs.

FREQUENCY RESPONSE

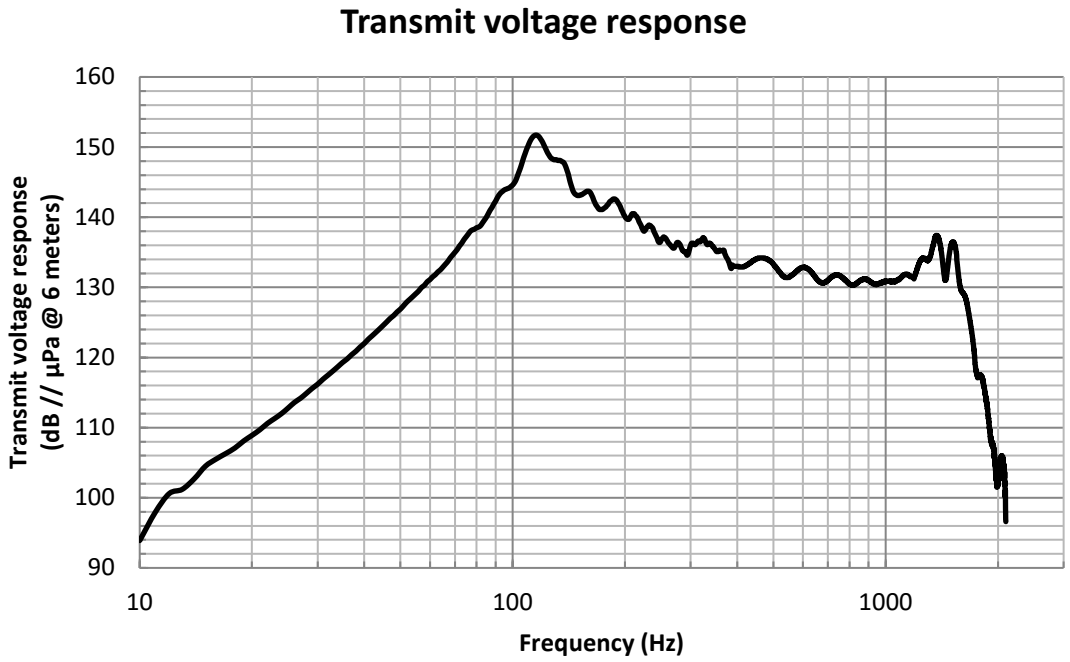

APPENDIX C. UW30 UNDERWATER LOUDSPEAKER

SPECIFICATIONS

Versions Available:
UW30 ..... 50 feet of cable (15.24 m)
System Type: ..... Underwater loudspeaker system
Frequency Response: ..... 100-10,000 Hz
Power Handling, (500-5,000 Hz pink noise): ..... 30 watts
Impedance: .....Nominal: 8 ohms
Dispersion: .....Omnidirectional underwater
Operating Depth: ....Up to 3.0 m (10.0 ft) below surface of water
Recommended Installation Depth: ..... 1.2 m (4.0 ft)
Finish: .....Pool blue
Dimensions,
Overall Diameter: .....182.6 mm (7.19 in.)
Depth: .....66.3 mm (2.61 in.)
Shipping Weight: .....1.8 kg (4.0 lb)

DIMENSIONS

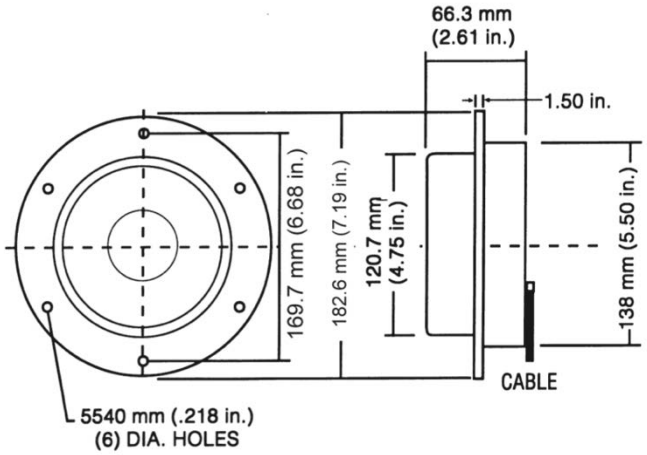

THIS PAGE INTENTIONALLY LEFT BLANK

APPENDIX D. CANTED SENSORS MATLAB CODE

```
% Author: German Da Re
% Rev 18 Aug 2018
% Code to read raw data acquired by two MFLI Lock-in Amplifiers in CSV
% form.
% One rotation is used to acquire the data.
% Manual Correction of the mounting angle error due to mounting error on
% the B&K turntable.
% The data is sample with 121 point to build a Look-up table between -60
% deg to 60 deg.
% Plots of the raw data and the Canted Angle relation signal (difference
% over the sum) that is
% (Left-Right)/(Left + Right).


clear all; close all;clc

% Import Raw data from the text files
[Time1,Left] = MFLI_readfile('dev3676_30deg.txt');
[Time2,Right] = MFLI_readfile('dev3686_30deg.txt');

% Define length of the vectors
L=min(length(Left),length(Right));

% Resize vector to the same length of useful data
time=Time1(5:L);
Left=Left(5:L); % left Sensor
Right=Right(5:L); % Right sensor

% Normalize vectors
Normalize=[Left/max(Left),Right/max(Right)];

% Search start time of the measurement
grad=gradient(Left);
pulse=grad>max(grad)*.1; % trigger pulse
start=find(Time1==min(Time1(pulse)));
end1=find(Time1==max(Time1(pulse)));

% Resize Matrix
Left= Left(start:end1,:);
Right= Right(start:end1,:);
Normalize= Normalize(start:end1,:);

% Unnormalize Matrix of vectors
Unnormalize=[Left,Right];
data=abs(start-end1);
```

```
% Reshape Matrix up to 360 degrees
Unnormalize=Unnormalize(1:data,:);
Normalize=Normalize(1:data,:);
deg=linspace(0,360,data);
deg2=linspace(-180,180,data);
deg3=linspace(-180,180,length(Right));
deg4=linspace(-70,70,1000); %degrees to plot the fit

% Build on matrix with degree correlation
MEMS_norm=[deg',Normalize];
MEMS_raw=[deg',Unnormalize];

% Anechoic Chamber Angle Correction
degree=data/360;
degshift= 0;% 0 -1.7%-9.369;       % angle correction in degrees for
MEMS_norm=circshift(MEMS_norm,floor(degshift*degree));
MEMS_raw=circshift(MEMS_raw,floor(degshift*degree));

% atan aproximation
Angle=(Left-Right)./(Left+Right);
V_L=MEMS_raw(:,2);
V_R=MEMS_raw(:,3);
Angle2=(V_L-V_R)./(V_L+V_R);

% Sample data Look-up table construction
N=121; % number of sample
thetasample=linspace(-60,60,N);
n=1:N;
n=n';
for i=1:length(thetasample)
    index(i)=min(deg2((deg2-thetasample(i))>=0));
    sample(i)=Angle2(index(i)==deg2);
end
thetasample=thetasample';
sample=sample';

% Look-up table
error=abs(.2631*tan(30*pi/180)*tan(thetasample*pi/180)-sample);
table1=table(n,thetasample,sample,error);
Angle_rad=thetasample*pi/180;

% Fitting
alpha=[0.223  0.2812 0.2368]
L_theta=MEMS_raw(find(MEMS_raw(:,2)==min(MEMS_raw(MEMS_raw(:,1)>180,2))))-
180+degshift;
R_theta=MEMS_raw(find(MEMS_raw(:,3)==min(MEMS_raw(MEMS_raw(:,1)>180,3))))-
180+degshift;
theta_diff=abs(L_theta-R_theta);
```

```
% Plots
figure(1)
subplot (1,2,1)
plot(deg2,MEMS_raw(:,2),'r',deg2,MEMS_raw(:,3),'b','Linewidth',1.5)
xlabel('Angle (deg)')
ylabel('Amplitude (V)')
legend('Left','Right')
grid on
xticks([-180:60:180])
xlim([-180,180])
axis square

hold on
x_points = [R_theta, R_theta, L_theta, L_theta];
y_points = [0, max(ylim), max(ylim), 0];
color = [0, 0, 1];
a = fill(x_points, y_points, color);
a.FaceAlpha = 0.1;
text(L_theta+1,.03,strcat('\theta_{eff-
off}=',num2str(round(theta_diff,1)),'º'))
set(gca,'Fontsize',14)
%
subplot (1,2,2)
plot(deg2,Angle2,'k','Linewidth',1.5)
hold on
plot(thetasample,sample,'o','Color',[0.4660, 0.6740, 0.1880])
xlim([-100,100])
xticks([-100:25:100])
ylabel('Amplitude')
xlabel('Angle (deg)')
grid on

hold on
plot(deg4,alpha(1)*tan(30*pi/180)*tan(deg4*pi/180),'r','linewidth',1.5)
plot(deg4,tan(theta_diff/2*pi/180)*tan(deg4*pi/180),'Color','b','linewidth',1.5
)
ylim([-1,1])
legend('Angle','Sample           Look-up           table','Fit           =\alpha
tan(\theta_{off})tan(\theta)'...
    ,'Fit= tan(\theta_{eff-off}/2)tan(\theta)','location','northwest')
axis square
set(gcf,'Position',[0 450 880 400])
set(gca,'Fontsize',14)
```

THIS PAGE INTENTIONALLY LEFT BLANK

LIST OF REFERENCES

[1] N. J. Wade and D. Diana, "Early binaural research," *Acoustics Today*, July 2008. [Online]. Available: http://deutsch.ucsd.edu/pdf/AT-2008_4_3.pdf

[2] D. Wang and G. J. Brown, *Computational Auditory Scene Analysis: Principles, Algorithms, and Applications*, Wiley-IEEE Press, 2006.

[3] R. N. Miles, D. Robert, and R. Hoy, "Mechanically coupled ears for directional hearing in the parasitoid fly *Ormia ochracea*," *J. Acoust. Soc. Am.*, vol. 98, no. 6, pp. 3059–3070, December 1995.

[4] D. Wilmott et al., "Bio-inspired miniature direction finding acoustic sensor," *Sci. Rep. 6, 29957*, Jun. 2016.

[5] A. Ishfaque and B. Kim, "Fly *Ormia ochracea* inspired MEMS directional microphone: A review," *IEEE Sensors Journal*, vol. 18, no. 5, pp. 1778–1789, 2018.

[6] R. N. Miles, Q. Su, W. Cui, and M. Shetye, "A low-noise differential microphone inspired by the ears of the parasitoid fly *Ormia ochracea*," *The Journal of the Acoustical Society of America*, vol. 125, no. 4, p. 2013–2026, April 2009.

[7] M. L. Kuntzman and N. A. Hall, "Sound source localization inspired by the ears of the *Ormia ochracea*," *Applied Physics Letters*, vol. 105, no. 033701, pp. 1–4, June 2014. [Online]. doi: 10.1063/1.4887370

[8] M. Touse, "Fabrication of a microelectromechanical directional sound sensor with electronic readout using comb fingers," *Appl. Phys. Lett.*, vol. 96, no. 6, 2010.

[9] M. Touse, "Design, fabrication, and characterization of a microelectromechanical directional microphone," Ph.D. dissertation, Dept. of Physics, Naval Postgraduate School, Monterey, CA, 2011. [Online]. Available: https://calhoun.nps.edu/handle/10945/10762

[10] R. H. Downey, "Toward A micro-scale acoustic direction-finding sensor with integrated electronic readout," Ph.D. dissertation, Dept. Physics, Naval Postgraduate School, Monterey, CA, June 2013. [Online]. Available: https://calhoun.nps.edu/handle/10945/34658

[11] J. D. Roth, “Integration of a high sensitivity MEMS directional sound sensor with readout electronics,” M.S. thesis, Dept. Physics, Naval Postgraduate School, Monterey, CA, December 2012. [Online]. Available: https://calhoun.nps.edu/handle/10945/27897

[12] W. D. Swan, “Bio-inspired MEMS direction finding acoustic sensor for air and underwater applications,” M.S. thesis, Dept. Physics, Naval Postgraduate School, Monterey, CA, 2016.

[13] J. D. Collins, “Bio-inspired MEMS underwater direction finding acoustic sensor,” M.S. thesis, Dept. Physics, Naval Postgraduate School, Monterey, CA, 2017.

[14] L. E. Kinsler, A. R. Frey, A. B. Coppens, and J. V. Sanders, *Fundamentals of Acoustics*, John Wiley & Sons, Inc., 4th edition, 2000.

[15] “COMSOL Multiphysics,” COMSOL Multiphysics, 12 July 2016. [Online]. Available: https://www.comsol.com/blogs/theory-of-thermoviscous-acoustics-thermal-and-viscous-losses/

[16] M. A. Hopcroft, N. D. William, and K. W. Thomas, “What is the Young’s modulus of silicon?” *Journal of Microelectromechanical Systems,* vol. 19, no. 2, pp. 229–238, April 2010.

[17] A. Cowen, G. Hames, D. Monk, S. Wilcen, and B. Hardy, SOIMUMPs Design Handbook v5.0, MEMSCAP Inc., 2008.

[18] U. S. A. G. (NAVY), “U.S. Navy Requirements for Underwater Sound Transducer Calibration and Test Facilities,” U.S. Navy, Washington, D.C., 1963.

[19] Google, “San Diego.” [Online]. Available: https://www.google.com/maps/place/Transdec+Rd,+San+Diego,+CA+92106/@32.7018956,-117.2486737,150a,35y,313.84h,47.56t/data=!3m1!1e3!4m5!3m4!1s0x80deabf1f5c7563b:0xdc2b1b92e20c73cb!8m2!3d32.703068!4d-117.2499658

[20] L. J. Ziomek, *An Introduction to Sonar Systems Engineering*, Monterey, California: CRC Press, 2016.

[21] D. Wilmott, “Direction finding using multiple MEMS acoustic sensors,” M.S. thesis, Dept. Physics, Naval Postgraduate School, Monterey, CA, September 2015. [Online]. Available: https://calhoun.nps.edu/handle/10945/47345

[22] Z. I. AG, “MFLI User Manual,” Zurich Instruments AG, 22 December 2017. [Online]. Available: https://www.zhinst.com/sites/default/files/ziMFLI_UserManual_49900.pdf. [Accessed 24 July 2018]

THIS PAGE INTENTIONALLY LEFT BLANK

INITIAL DISTRIBUTION LIST

1. Defense Technical Information Center
   Ft. Belvoir, Virginia

2. Dudley Knox Library
   Naval Postgraduate School
   Monterey, California